Multi-Objective Optimization for Wave Energy Converter Based on Robust-Stochastic Control for Uncertainty and Dynamic Order Adaptive Runge-Kutta

Runhao Liu and Ziming Chen

Abstract—To optimize the energy output of wave energy converters (WECs) in complex ocean environments, a novel multi-objective robust-stochastic strategy that integrates uncertainty modeling to address the dynamics of ocean waves is presented. We introduce the dynamic order adaptive Runge-Kutta (DOARK) method for more efficient solution of kinetic equations. The optimization strategy seeks to maximize power output while minimizing systematic damage. First, we develop kinetic formulations for the proposed WEC and incorporate stochastic terms for a more accurate description in volatile conditions. The control process is optimized using a multiobjective approach with a cost function that balances output power and damage, solved via the ε -constraint method. An adaptive algorithm is applied to adjust step size, enhancing the Runge-Kutta method. In our approach, step size is iterated based on damping coefficient ranges. Simulation results demonstrate that the proposed strategy improves output power by 12.34% and reduces systematic damage by 15.65%, compared with traditional methods, which demonstrates the advantage of the proposed method.

Index Terms—Wave energy converter, uncertainty modeling, dynamic order adaptive Runge-Kutta, robust-stochastic control, multi-objective optimization

I. INTRODUCTION

NERGY is an essential demand for the development of the global economy. Meanwhile, efficient economic increase relies on sufficient energy utilization. However, many countries are facing challenges including depletion of fossil fuels and environmental pollutions [1]. Without the solution of these obstacles, the economy will be trapped in a standstill. Therefore, the use of renewable energy evokes keen attention around the world. Wherein, the marine renewable energy, wave energy in particular, is one of the most prospective renewable energy with extensive potentials in the economic development [2].

Manuscript received: 4 January 2025; revised: 17 April 2025; accepted: 6 May 2025. (Corresponding author: Runhao Liu.)

Citation: R. Liu and Z. Chen, Multi-objective optimization for wave energy converter based on robust-stochastic control for uncertainty and dynamic order adaptive Runge-Kutta, *Int. J. Intell. Control Syst.*, 2025, 30(2), 123–143.

Runhao Liu is with Polytechnic Institute, Zhejiang University, Hangzhou 310015, China (e-mail: runhaoliu@zju.edu.cn).

Ziming Chen is with School of Social and Public Administration, East China University of Science and Technology, Shanghai 200237, China (e-mail: zimingchen276@gmail.com).

Digital Object Identifier 10.62678/IJICS202506.10155

Based on surveys, the theoretical usable resource of wave energy is estimated nearly 32,000 TWh/year [3]. Furthermore, the average of the densities of wave energy is estimated 2.00–3.00 kW/m² while the solar energy and wind energy are 0.17 and 0.50 kW/m², respectively [4]. Therefore, as a widelyused tool in wave energy collection, the wave energy converters (WECs) can provide a significant portion of converting the wave energy into power output [5]. To capture energy more efficiently, control optimizations are accessible enhancement without excessive extra cost. Nevertheless, the interference of volatile waves can be one of the most crucial challenges, which may cause unacceptable systematic damage. Meanwhile, volatile waves cause more kinetic motion, which leads to more energy output. Therefore, the comparison between the energy output and systematic damage is a problem to overcome.

Recently, much attention has been paid to the novel physical modifications of WECs to overcome the problems in unstable ocean. To cope with the uncertainty, establishing models with interference is proved as a valid method. Aderinto and Li [6] proposed a self-adjustable wave energy converter that altered its inertia by ballasting and de-ballasting with seawater. Clemente et al. [7] developed and assessed a wave energy conversion technology which could be integrated into seaport breakwaters. Devin et al. [8] designed a pitch resonator power take-off (PTO) system using a geared flywheel system for power generation. Al Shami et al. [9] proposed a novel wave energy harvester using a Scotch Yoke mechanism to convert the heave motion of a buoy into rotational energy for an offthe-shelf rotary generator. In Ref. [10], a multi-dimensional wave energy converter that realizes wave-to-power via 6 parallel hydraulic cylinders is proposed. Zhang et al. [11] constructed a multi-degree of freedom decoupled WEC and performed optimization in varying wave conditions.

Simultaneously, the development of new optimization strategy for WEC is crucial for a more accessible wave energy utilization. Owing to the characteristic of non-linear and unstable characteristic of waves and marine environment, wave energy output is unpredictable for long time-horizons. Avila et al. [12] proposed a mixture density network-based method for forecasting the capabilities of WEC at offshore and nearshore points, which fitted bivariate Weibull

distributions to spectral significant wave height and mean peak period data. Adibzade and Akbari [13] presented a transfer function (TF) over a desired range of wave frequencies to assess multi-body floating wave energy converter (MBFWEC) operating, which could be deployed in complex sea states. Fan et al. [14] proposed a model to simulate the entire process of waves to power grid of the WEC with a controllable-valve buoy. This method can evaluate the power generation capabilities of WEC under the complex sea conditions. In Ref. [15], the wave roller and oyster WEC are improved by the wave tower wave surge converter to reduce area of effect. Quilodrán-Casas et al. [16] proposed a machine learning based synthetic data generated method for WEC performance evaluation. This method can have a speed up from 5 to 6 orders of magnitude for the new samples production. Adibzade and Akbari [17] evaluated the energy output of multi-body floating wave energy converters in complex sea states with multi-peak wave spectra with a two-dimensional (2D) transfer function based innovative method. This method prevails in multi-directional sea states and the function of wave directionality in power calculations is highlighted in this work. To deal with the challenge of optimizing the efficiency of WEC on a regional scale, Mehdipour et al. [18] developed a hill climb-explorative grey wolf optimizer, which was a hybrid algorithm combining local search and swarm-based global optimization strategies. Zhang et al. [19] proposed a chaos-based differential evolutionary algorithm for evaluating the optimal buoy arrangement effectively and promptly. This algorithm consists of excavation, balancing, and recycling layers, which is a threelayer information structure. Compared with four traditional mainstream algorithms, a real-time controller method is developed by Zhang et al. [20]. The method integrated with a long short-term memory recurrent neural network wave prediction model, which is more compatible under irregular waves. Xu et al. [21] proposed a numerical model based on 6 degrees of freedom for enhancing energy conversion efficiency of WEC and analyzed the effect of 9 types of motions.

The Runge-Kutta (RK) method is highly precise, stable, and capable of handling non-linear systems, making it suitable for complex wave dynamics in WEC research [22]. Runge-Kutta is highly emphasized in the research of wave energy. Liu et al. [23] integrated Runge-Kutta fourth-order (RK-4) method to solve the response and capture performance of the evaluation of mean annual capture width ratio capacity of the oscillating wave surge converters in the situation that the wave was irregular. Mirzaei et al. [24] discretized the boundary conditions with RK-4. He et al. [25] proposed a weighted RK discontinuous Galerkin method and extended this method to solve the elastic wave equations in 2D transversely isotropic media. Chen et al. [26] proposed an RK-4-based solution method to solve the motion equations of WEC.

Taking the irregular ocean environment into consideration, the multi-objective optimization is required to realize a tradeoff of multiple elements for non-linear problems [27]. Hoffmann et al. [27] introduced a multi-objective model predictive control approach for WEC based on dielectric elastomer generator, whose order was to maximize energy harvested from ocean waves while minimizing the damage accumulated by the dielectric elastomer generator. Carapellese et al. [28] proposed a dynamic analysis and performance assessment of the inertial sea wave energy converter with nonlinear model to achieve energy-maximizing control and energy absorption improvement. Cheng et al. [29] presented a hybrid WEC that integrated an oscillating water column and an oscillating buoy, which was installed within a π -type breakwater to enhance the floating hydrodynamic performance. Shadmani et al. [30] utilized two primary objective functions of energy production based on wave conditions and the layout of WEC arrays for reducing interference between the devices to improve global efficiency. Cheng et al. [31] explored the feasibility of integrating very large floating structures with multiple WECs combined with oscillating water columns and oscillating flaps. Additionally, Gu et al. [32] concentrated on the optimization of cost and emission. Rahimi et al. [33] paid attention to the two-objective optimization of the WECs' dimensions and the power PTO parameters. By adjusting the production torque within the PTO, Vakili et al. [34] optimized the energy efficiency of Pelamis WEC. Based on survey, multi-objective optimization plays a crucial role in addressing the complex non-linear optimization problems of WECs by balancing conflict objectives.

The surveyed literature reveals that while physical modifications show promise, their high complexity and cost hinder practical use. Recent optimization strategies focus on multi-dimensional objectives, but neglect the impact of volatile wave conditions, highlighting the need to consider non-linear and unstable factors. We address these issues by introducing stochastic perturbation elements to improve system dynamics under uncertainty. Hybrid robust control strategy and frequency domain analysis are used to assess uncertainty impacts. Additionally, the RK method's accuracy needs improvement, and existing models largely assume predictable, periodic wave motion, overlooking the instability of ocean environments, especially in harsh weather regions. Recent researches have emphasized the significance of dynamic optimization [35]. Therefore, to balance accuracy and cost, we propose a dynamic order adaptive Runge-Kutta (DOARK) approach, which adjusts step size and order. A multi-objective robust-stochastic strategy is also introduced to mitigate damage from environmental complexity, solving the stochastic multi-objective problem and selecting the optimal trade-off via a fuzzy membership function. The highlights of this paper are summarized as follows:

- (1) Stochastic perturbation term is concluded in the model for comprehensive consideration about uncertainty for depicting the output of energy more accurately. Thus, our proposed model will be more suitable for complex ocean environment.
- (2) The DOARK is developed to solve the model, which realizes the mechanism for dynamic orders selection. Step with different sizes in scenarios with different volatility is adapted and the errors will be reduced in iteration process.
- (3) A multi-objective robust-stochastic strategy is conducted

for the simultaneous optimization of the maximum of output power and the minimum of systematic damage. Meanwhile, the proposed strategy is capable of controlling the parameters concerning the systematic damage. This method minimizes the total systematic damage and mitigates the effect of the uncertain parameters.

The rest of this paper is as follows. Section II describes the mathematical model of our proposed WEC, including the description of kinetic motions and the energy output. Meanwhile, the model integrated with uncertainty is constructed in detail. Section III presents methods for searching the numerical solution for the established model. The improved DOARK is constructed in Section IV, as well as our multi-objective robust-stochastic optimization strategy is introduced. The results of simulation are also demonstrated in Section IV for evaluating the effect of model with uncertainty and the DOARK. Finally, Section V presents some final remarks and conclusions.

II. PROBLEM FORMULATION

Our proposed WEC is depicted in Fig. 1. The proposed WEC contains buoy, vibrator, central shaft, and power takeoff system. The PTO unit is integrated with a permanentmagnet linear generator with a rotary damper. Incident waves excite coupled heave and small amplitude pitch of the buoy. These motions are transmitted along the shaft to the vibrator, in which the relative translational and rotational displacements drive the PTO and are directly converted into three phases electrical power. The hydro mechanical dynamics are represented by a four-degree-of-freedom model incorporating buoy mass and added mass, hydrostatic restoring stiffness, frequency-dependent radiation damping, and a time-varying PTO damping coefficient c(t). Although energetic sea states increase instantaneous power extraction, they also elevate structural loads and promote cumulative fatigue damage. Consequently, the control objective considered in this work is to schedule c(t), so that the mean absorbed power is maximized while the damage remains below its permissible threshold, thereby achieving an optimal compromise between energy yield and structural integrity.

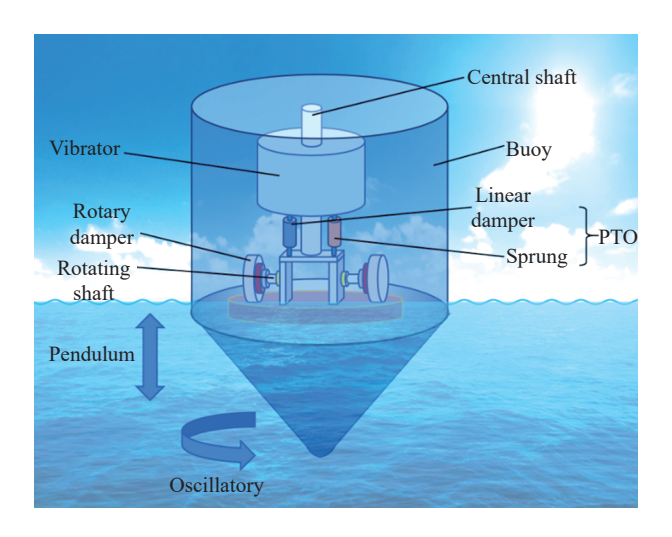


Figure 1 Overall structure of the proposed WEC model.

III. MODELING

A. System Modeling

When the WEC is floating on the water, it is influenced by hydrostatic recovery force, which is the restoring force that automatically acts on an object to push it back to its original equilibrium attitude after being pushed away from its equilibrium draft position by an external force because of an imbalance in the moments generated by buoyancy and gravity. The hydrostatic recovery of buoy F_1 is shown in Eqs. (1) and (2).

$$F_1 = F_2 - (G_1 + G_2) = V(x_{1,t})g \tag{1}$$

$$V(x_{1,t}) = \begin{cases} \pi R x_{1,t}, x_{1,t} \le 2.0; \\ 2\pi + 0.52\pi (2.8 - x_{1,t})^3, 2.0 < x_{1,t} \le 2.8 \end{cases}$$
 (2)

where F_2 is the buoyancy, R is the radius, and G_1 and G_2 are the gravities of vibrator and buoy, respectively. The $x_{1,t}$ is the replacement of buoy. The wave exciting force is also included in the motion of WEC. Note that f represents amplification, and ω represents the incident wave frequency, and t is time. Thus, the wave exciting force is shown in F_3 .

$$F_3 = f\cos(\omega t) \tag{3}$$

The wave-making resistance on the float is the resistance caused by the ocean wave when the buoy is moving in a pendulum motion, which is proportional to the velocity of the floating body pendulum swing and opposite in direction. The wave-making resistance F_4 is given by

$$F_4 = q \cdot v_{2,t} \tag{4}$$

where q is the resistance coefficient and $v_{2,t}$ is the move speed. Not only will the buoy be pushed by the forces, but the surrounding fluids also need to be moved. The force that drives a floating body in a rocking motion must not only drive the floating body in motion, but also the fluid around the floating body. If the floating body is to gain acceleration in the waves, an additional force needs to be applied, i.e., an additional inertial force m_3 , therefore, the force of added mass F_5 is given as

$$F_5 = m_3 \frac{d^2 x_{1,t}}{dt^2} \tag{5}$$

The oscillator is in reciprocating motion along the central axis, always with a spring attached to one end, which exerts a force during the pendulum motion. The amount of this force is proportional to the difference in displacement of the buoy and the vibrator. The magnitude of the elastic force exerted on the vibrator F_6 is shown in Eq. (6).

$$F_6 = k_1(x_{1,t} - x_{2,t} + x_0) \tag{6}$$

where $x_{2,t}$ is the displacement of the vibrator, and x_0 represents the initial spring compression. The spring coefficient is written as k_1 . When the vibrator and the buoy move relative to each other, the linear damper produces a damping force, which is proportional to their relative velocity. Thus, the damping force F_7 is expressed as

$$F_7 = k_2 \cdot (v_{1,t} - v_{2,t}) \tag{7}$$

where the damping coefficient of the linear damper is written as k_2 . The movement speeds of the buoy and vibrator are denoted as $v_{1,t}$ and $v_{2,t}$, respectively.

Under the action of waves, the buoy not only undergoes vertical oscillations, but also experiences longitudinal motion from side to side. At this moment, the central axis of the buoy is subjected to the moment of force exerted by the waves. In this more complex scenario, the determination of the buoy's center of gravity becomes necessary. As illustrated in Fig. 2, the center of gravity O is located on the central axis, as both the buoy and vibrator are rotational bodies. Denote the heights of the conical and cylindrical sections as H_1 and H_2 , respectively, and the height of the vibrator as H_3 . We introduce h_4 as the distance between point O and the top of the conical and cylindrical sections, while h_5 represents another relevant height parameter. Let m_1 and m_2 denote the masses of the buoy and the vibrator, respectively. Furthermore, the masses of the conical and cylindrical sections of the buoy are given by m_4 and m_5 . Consequently, the center of mass of the buoy is determined as Eq. (8).

$$h = h_4 \cdot m_4 - h_5 \cdot m_5 \tag{8}$$

Based on the equilibrium axis theorem, the moment of inertia J_4 is given by

$$J_4 = J_1 + J_2 + m_4 \cdot h_4^2 + m_5 \cdot h_5^2 \tag{9}$$

where J_1 and J_2 are the moments of inertia of the cylindrical and conical parts, respectively.

Equation (10) describes the moment of inertia of the vibrator. When the vibrator has a straight-line mass distribution along its center of mass axis of gyration, its moment of inertia J_5 is given as

$$J_5 = \frac{m_2}{2} \left(r^2 + \frac{1}{6} H_3^2 \right) \tag{10}$$

where r is the radius of the vibrator.

The vibrator undergoes longitudinal oscillation around the bottom rotating axis, which is located on the interface surface and is parallel to the rotating shaft frame. Given that the height of pedestals and rotating shaft can be neglected, the distance between the center of gravity and the center of the circular interface, denoted as l, is expressed as

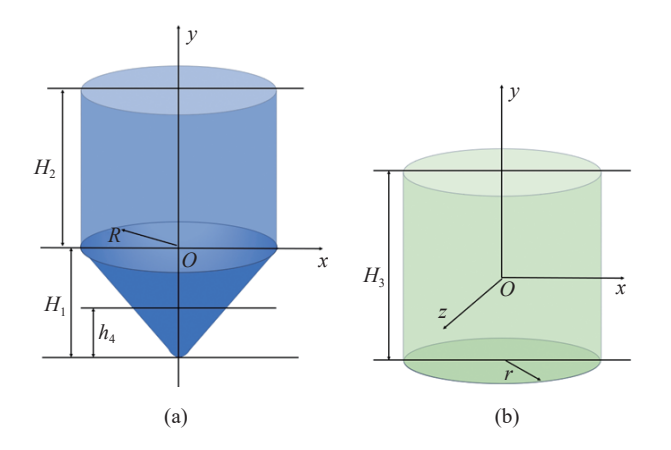


Figure 2 Schema of the structure of buoy and vibrator.

$$l = x_{2,t} - x_{1,t} + x_{00} + \frac{H_3}{2}$$
 (11)

where x_{00} represents the original length of the spring.

By applying the parallel-axis theorem, a more precise representation of the vibrator's moment of inertia J_6 is obtained.

$$J_6 = J_5 + m_2 l (12)$$

Finally, the hydrostatic recovery moment of the buoy $M_{\rm hr}$ is given by

$$M_{\rm hr} = c_{\rm hr} \cdot \theta_1 \tag{13}$$

where the angular displacement between the axis of the vibrator and the buoy is denoted as θ_1 , while θ_2 represents the angular displacement between the plumb line and the axis of the buoy. Additionally, the coefficient of the hydrostatic recovery moment is denoted as $c_{\rm hr}$.

The oscillatory motion of the wave energy converter is driven by the wave-exciting force F_3 and the wave-exciting moment M_{we} , which is expressed in Eq. (14).

$$M_{\rm we} = L\cos(\omega t) \tag{14}$$

where L is defined as the amplification factor of the oscillatory motion.

When considering the oscillatory motion, the moment of wave-making resistance cannot be ignored because of the resistance caused by waves, which opposes the oscillatory motion of the floating buoy. The moment of wave-making resistance is proportional to the angular velocity of the float's oscillation. Synonymous with the force described in F_4 , the moment of wave-making resistance, denoted as $M_{\rm WMR}$, acts in the opposite direction to the angular velocity of the buoy w_1 . This moment also has a proportional coefficient q_2 . Thus, $M_{\rm WMR}$ is defined as

$$M_{\text{WMR}} = q_2 \cdot w_1 \tag{15}$$

As for the oscillatory motion of the WEC, the torque of the rotary spring M_{TRS} is given by

$$M_{\text{TRS}} = k_3(\theta_1 - \theta_2) \tag{16}$$

where k_3 represents the stiffness of the rotary damper.

Similar to F_7 , the torque of the rotary damper M_{TRD} is defined as

$$M_{\text{TRD}} = k_4(w_1 - w_2) \tag{17}$$

where k_4 is the damping coefficient of the rotary damper, and w_2 is the velocity of the vibrator.

When the buoy undergoes longitudinal oscillatory motion, the spring tilts. Consequently, the pressure exerted by the object on the spring is reduced, effectively creating an upward-tilted force pulling the spring upward. The force in the vertical direction is analyzed by decomposing it orthogonally into the force equation of the pendulous oscillatory motion. The elastic force of the spring F_6' is defined as

$$F_6' = mg - mg\cos(\theta_1 + \theta_2) \tag{18}$$

When the vibrator and buoy are in longitudinal motion, the damping force is tilted instead of acting purely in the vertical direction. In this case, the damping force of the vibrator F'_7 follows

$$F_7' = -F_7 \tag{19}$$

Based on the analysis of mechanical forces, a system of equations for dynamics is formulated. First, the motion of the buoy is described by Eqs. (20) and (21), considering only the pendulum motion. The floating buoy is influenced by wave-exciting force, wave-making resistance, hydrostatic recovery force, and buoyancy. The two equations below indicate that the acceleration of the floating buoy is affected by the variation of buoyancy with depth.

$$(m_1 + m_3)\frac{d^2x_{1,t}}{dt^2} = f\cos(\omega t) - c\frac{dx_{1,t}}{dt} - V(x_{1,t})\rho g$$
 (20)

where the buoyancy function $V(x_{1,t})$ is defined as

$$V(x_{1,t}) = \begin{cases} \frac{2}{3}\pi(2.8 - x_{1,t})^3, \ 2.0 \le x_{1,t} \le 2.8; \\ 0, \text{ otherwise} \end{cases}$$
 (21)

where c represents the general resistance coefficient.

For the vibrator, the effects of gravity, spring force, and damping force are considered. The gravity counteracts the initial spring force, which allows the system to be simplified by assuming that the original length of the spring remains unchanged over time, and gravity does not contribute to the vibrator's motion. Thus, Eq. (22) represents the dynamic equation governing the motion of the vibrator, emphasizing the interaction between the floating buoy and the vibrator through the spring coefficient and the damping coefficient of the linear damper.

$$m_2 \frac{\mathrm{d}^2 x_{2,t}}{\mathrm{d}t^2} = -k_1 (x_{2,t} - x_{1,t}) - k_2 \left(\frac{\mathrm{d}x_{2,t}}{\mathrm{d}t} - \frac{\mathrm{d}x_{1,t}}{\mathrm{d}t} \right) \tag{22}$$

In the scenario that only pendulum motion is considered, the buoy and vibrator move vertically, and their initial positions are at the origin. This study assumes that both objects are floating on the water, so their initial velocity is zero. Consequently, the simultaneous equations describing the initial conditions of displacement are given as

$$\begin{cases} x_{1,t}(0) = 0, \\ x_{2,t}(0) = 0, \\ \frac{dx_{1,t}(0)}{dt} = 0, \\ \frac{dx_{2,t}(0)}{dt} = 0 \end{cases}$$
 (23)

These overall equations are obtained by applying Newton-Euler balances to the heave-pitch motions of the buoy and the surge-roll motions of the internal mass. Their inertial contribution is merged the structural mass with the frequency-dependent added mass. Then, the harmonic wave-excited force or torque, and the velocity-proportional terms are superposed to account for radiation damping and PTO damping effects. Meanwhile, their displacement-proportional term is used to represent hydrostatic restoring force. The relative displacement and velocity terms are conducted to

express the coupling spring and damper between the buoy and the vibrator. These contributions form a set of four coupled second-order differential equations providing the complete dynamical model of the WEC system.

One of the primary contributions of this work is the introduction of minor perturbations into the model to account for uncertainty. To analyze the system's response to small perturbations, a linearization process is applied. The perturbation terms are defined as $\delta x_{1,t}$ and $\delta x_{2,t}$. Accordingly, the perturbed equations are given by

$$\begin{cases} x_{1,t} = x_{1,0} + \delta x_{1,t}, \\ x_{2,t} = x_{2,0} + \delta x_{2,t} \end{cases}$$
 (24)

Substituting Eq. (24) into Eqs. (20) and (22), the system is linearized, yielding Eq. (25)

$$\begin{cases} (m_1 + m_3) \frac{d^2 x_{1,t}}{dt^2} = f \cos(\omega t) - c \frac{d x_{1,t}}{dt} - k_1 (\delta x_{2,t} - \delta x_{1,t}), \\ m_2 \frac{d^2 (\delta x_{2,t})}{dt^2} = -k_1 (\delta x_{2,t} - \delta x_{1,t}) - k_2 \left(\frac{d (\delta x_{2,t})}{dt} - \frac{d (\delta x_{1,t})}{dt} \right) \end{cases}$$
(25)

For further analysis of the robustness of the proposed WEC system, a frequency domain analysis is conducted. Based on the Laplace transform, the transformation function is constructed, leading to the auxiliary Eq. (26). Here, s represents the complex number of frequency response. The coefficient c denotes the resistance coefficient, which accounts for the effect of resistance when the system moves with water. The transformed displacements of the floating buoy and vibrator, denoted as $X_{1,t}(s)$ and $X_{2,t}(s)$, respectively, are expressed using the Laplace transform.

$$\begin{bmatrix} (m_1 + m_3)s^2 + cs + k_1 & -k_1 \\ -k_1 & m_2s^2 + k_2 \end{bmatrix} \begin{bmatrix} X_{1,t}(s) \\ X_{2,t}(s) \end{bmatrix} = 0 \quad (26)$$

Thus, this modification enables a more comprehensive consideration of the equilibrium and stability of the system, enhancing the model's robustness against perturbations and improving its accuracy in reflecting the real physical behavior. For instance, the system response characteristics can be optimized by adjusting parameters k_1 and k_2 to ensure the stability of the proposed system. Furthermore, the dynamic behavior of resonant frequency additions can be investigated through parameters f and ω . Additionally, the auxiliary equation formulated for frequency domain analysis is fundamental for studying resonance phenomena. Therefore, the proposed model, which incorporates minor perturbations and linearization, provides a more comprehensive understanding of the coupling dynamics between the buoy and the vibrator.

Based on the kinetic models established above to describe the pendulum motions of the proposed WEC, oscillatory motion must be considered for further analysis of factors, such as wave force, gravity, and buoyancy. Herein, c_i is utilized to represent the resistance coefficient in corresponding situations. The influence of waves acting on the buoy and vibrator is modeled as two disturbance terms, D_1 and D_2 ,

respectively. Consequently, the kinetic equations governing the motion of the floating buoy and vibrator are given by

$$(m_1 + m_3) \frac{d^2 x_{1,t}}{dt^2} = f \cos(\omega t) - c_1 \frac{d x_{1,t}}{dt} - V(x_{1,t}) \rho g + D_1$$
(27)

$$m_{2} \frac{d^{2} x_{2,t}}{dt^{2}} = m_{2}g(1 - \cos(\theta_{1} - \theta_{2})) - k_{1}(x_{2,t} - x_{1,t}) - k_{2} \left(\frac{dx_{2,t}}{dt} - \frac{dx_{1,t}}{dt}\right) + D_{2}$$
(28)

The corresponding phase constant ϕ_i is incorporated into the model. Thus, the disturbance terms are defined as

$$\begin{cases}
D_1 = D_{A1} \sin(k_1 x_{1,t} - \omega_{w1} t + \phi_1), \\
D_2 = D_{A2} \sin(k_2 x_{2,t} - \omega_{w2} t + \phi_2) + D_{\Gamma 1}
\end{cases}$$
(29)

where D_{A1} is the amplitude of the buoy's motion, and D_{A2} corresponds to that of the vibrator. Meanwhile, ω_{wi} represents the effect of the wave frequency on different components of the system. D_1 represents primary harmonic component of incident wave group acting on the buoy and D_2 is the combined effect of transmitted wave load plus in-body hydromechanical noise.

It is important to note that the primary disturbance acting on the floating buoy can be fully explained by wave harmonics. However, the vibrator is not only influenced by wave forces, but also by the motion of the buoy, as it is placed within the buoy's interior. Therefore, based on the mechanical force analysis, an additional noise component $D_{\Gamma 1}$ must be considered, where $D_{\Gamma 1} \sim \mathcal{N}(0, \sigma^2)$.

To more accurately characterize the state of the system in oscillatory motion, the relative inclination between the buoy and vibrator, caused by wave energy, is described as

$$\begin{cases} \delta\theta_{1} = \frac{D_{A1}}{k_{4}} \sin(k_{4}\theta_{1} - \omega_{w1}t + \phi_{1}), \\ \delta\theta_{2} = \frac{D_{A2}}{k_{3}} \sin(k_{3}\theta_{2} - \omega_{w2}t + \phi_{2}) \end{cases}$$
(30)

When the motion of the WEC exhibits both pendular and oscillatory behavior simultaneously, incorporating uncertainty and dynamic changes, the kinetic equation governing the oscillatory motion of the vibrator is transformed into

$$J_{2}\frac{d^{2}\theta_{2}}{dt^{2}} = -m_{2}g\sin(\theta_{2}) - k_{3}(\theta_{2} - \theta_{1}) - c_{3}\left(\frac{d\theta_{2}}{dt} - \frac{d\theta_{1}}{dt}\right) + D_{3}$$
(31)

where the disturbance term D_3 is defined as

$$D_3 = D_{A3}\sin(k_3\theta_2 - \omega_{w3}t + \phi_3) + D_{\Gamma 3}$$
 (32)

where D_{A3} represents the vibrator's amplitude of motion. Similarly, we assume that the perturbation term $D_{\Gamma 3}$ follows a standard normal distribution. For the same reason, the kinetic equation governing the floating body is given by

$$J_{1}\frac{d^{2}\theta_{1}}{dt^{2}} = -m_{1}g\sin(\theta_{1}) - k_{4}(\theta_{1} - \theta_{2}) - c_{4}\left(\frac{d\theta_{1}}{dt} - \frac{d\theta_{2}}{dt}\right) + D_{4}$$
(33)

where the disturbance term D_4 is defined as

$$D_4 = D_{A4}\sin(k_4\theta_1 - \omega_{w4}t + \phi_4) + D_{\Gamma 4}$$
 (34)

where $D_{\rm A4}$ represents the amplitude of motion of the buoy. Thus, the uncertainty simulated by D_3 is wave-induced overturning moment superposed with internal gearbox torsional jitter, while the restoring-moment fluctuation because of short-crested seas and slamming is simulated by D_4 .

In the present model, stochastic disturbance terms D_1 to D_4 are introduced to represent environmental uncertainty in a physically consistent and statistically calibrated manner. Each term acts on a specific degree of freedom, which includes buoy heave D_1 , vibrator heave D_2 , vibrator pitch D_3 , and buoy pitch D_4 . They are constructed from the first to the fourth dominant harmonics extracted from the measured wave-elevation spectrum. The harmonic amplitudes and phases are treated as zero-mean Gaussian random variables of which standard deviations scale with the significant wave height, while a small frequency perturbation is added to the pitch-related terms to capture short-crested sea effects. This formulation introduces multi-scale stochastic excitation without altering structural parameters, allowing the model to reproduce the statistical characteristics of both moderate and extreme sea states within a computationally tractable framework.

On this basis, we define a randomized interference term $D_{\rm u}$ to simulate the uncertainty in territorial waters under complex conditions, such as severe weather, unpredictable ocean currents, and varying wave frequencies. Herein, $D_{\rm s}$ represents the scalar factor used to control the intensity of stochastic perturbations. The randomized interference term $D_{\rm u}$ is modeled as a combination of random variables obeying a normal distribution $\mathcal{N}(0,\sigma_{\rm s}^2)$, as formulated in Eq. (35).

$$D_{\mathbf{u}} = D_{\mathbf{s}} \cdot \mathcal{N}(0, \sigma_{\mathbf{s}}^2) \tag{35}$$

Overall, we introduce the randomized interference term $D_{\rm u}$ into the kinetic equations of the floating body and vibrator. The simultaneous equations governing both pendular and oscillatory motion in the proposed WEC system are given in Eq. (36).

In specific, $D_{\rm u}$ is an unstructured disturbance term introduced to capture broadband environmental effects that are not represented by the harmonic terms D_1 to D_4 . It aggregates high-frequency wavelets, gust-induced pressure fluctuations, residual hydrodynamic interactions, and sensor noises. Mathematically, $D_{\rm u}$ is modelled as a zero-mean Gaussian process applied additively to each state equation. Its standard deviation is obtained from the residual energy of the measured wave spectrum after the first four peaks are removed and is further scaled by the scenario-dependent significant wave height. This formulation reproduces the stochastic envelope and rare high-intensity transients characteristic of severe sea states while maintaining numerical tractability.

The system governing the motion of the proposed WEC with the inclusion of disturbances is given by

$$\begin{cases}
(m_{1} + m_{3}) \frac{d^{2}x_{1,t}}{dt^{2}} = f\cos(\omega t) - c_{1} \frac{dx_{1,t}}{dt} - V(x_{1,t})\rho g + \\
D_{1} + D_{u} - u, \\
m_{2} \frac{d^{2}x_{2,t}}{dt^{2}} = m_{2}g\sin(\theta_{1} - \theta_{2}) - k_{1}(x_{2,t} - x_{1,t}) - \\
k_{2} \left(\frac{dx_{2,t}}{dt} - \frac{dx_{1,t}}{dt}\right) + D_{2} + D_{u} + u, \\
J_{1} \frac{d^{2}\theta_{1}}{dt^{2}} = -m_{1}g\sin(\theta_{1}) - k_{4}(\theta_{1} - \theta_{2}) - \\
c_{4} \left(\frac{d\theta_{1}}{dt} - \frac{d\theta_{2}}{dt}\right) + D_{4} + D_{u}, \\
J_{2} \frac{d^{2}\theta_{2}}{dt^{2}} = -m_{2}g\sin(\theta_{2}) - k_{3}(\theta_{2} - \theta_{1}) - \\
c_{3} \left(\frac{d\theta_{2}}{dt} - \frac{d\theta_{1}}{dt}\right) + D_{3} + D_{u}
\end{cases}$$
(36)

To enhance the stability of the model under complex conditions, a hybrid robust control strategy is incorporated. We develop a hybrid strategy combining sliding mode control (SMC) and robust control techniques to adapt to real-time variations and improve responsiveness to disturbances.

Define the state variable $z = x_{2,t} - x_{1,t}$, and introduce a closed-loop control system u. The control parameters k_a , c_a , and k_d are employed to regulate the system's response to disturbances and dynamic variations. Consequently, the control input u is defined as

$$u = -k_{a}z - c_{a}\frac{\mathrm{d}z}{\mathrm{d}t} + k_{d} \cdot D_{u}$$
 (37)

where u is applied to the relative translational degrees of freedom between the buoy and vibrator as inner force. The sign of the inner force appears with opposite values in the two equations to ensure consistency with the conservation of momentum. The first two equations in Eq. (36) can be subtracted to obtain the relative coordinate. As a result, the second-order dynamics of the relative displacement $z = x_{2,t} - x_{1,t}$ can be expressed as $\ddot{z} = -k_a z - c_a \dot{z} + k_d D_u$, corresponding to Eq. (37). u is essentially a realization of the equivalent spring-damping-disturbance compensation network in the translational subsystem, and its inclusion does not change the structure of the rotating subsystem.

A deeper analysis of the system's dynamic performance in complex sea conditions is required to assess its robustness and stability. Herein, the system's homeostatic behavior is evaluated based on the Lyapunov stability theory. The Lyapunov function is chosen to establish the dynamic performance index as

$$V(z) = \frac{1}{2}z^2 {38}$$

We derive the Lyapunov function, incorporating the control strategy to ensure convergence of the system state, yielding Eq. (39)

$$\frac{dV}{dt} = z \cdot (\dot{z} + u) = z \cdot \left(-k_{a}z - c_{a}\frac{dz}{dt} + k_{d}D_{u} \right),$$
s.t.,
$$\frac{dV}{dt} < 0$$
(39)

This condition guarantees the system's stability in complex sea conditions by selecting appropriate control parameters from Eq. (37). In other words, the proposed control strategy ensures the robustness of the system against random disturbances. For the solution, the initial conditions are given in Eq. (40).

$$\begin{cases} x_{1,t}(0) = x_{1,0}, \\ x_{2,t}(0) = x_{2,0}, \\ \frac{dx_{1,t}}{dt}(0) = v_{1,0}, \\ \frac{dx_{2,t}}{dt}(0) = v_{2,0}, \\ \theta_1(0) = \theta_{1,0}, \\ \theta_2(0) = \theta_{2,0}, \\ \frac{d\theta_1}{dt}(0) = \omega_{1,0}, \\ \frac{d\theta_2}{dt}(0) = \omega_{2,0} \end{cases}$$
(40)

Thus, by introducing a small perturbation term, the nonlinear problems involved in this study can be transformed into linear problems, as described in Eq. (41).

$$\begin{cases} x_{1,t} = x_{1,0} + \delta x_{1,t}, \\ x_{2,t} = x_{2,0} + \delta x_{2,t}, \\ \theta_1 = \theta_{1,0} + \delta \theta_1, \\ \theta_2 = \theta_{2,0} + \delta \theta_2 \end{cases}$$
(41)

By applying the Laplace transform, a frequency domain analysis of the system is conducted to obtain the transfer function, as described in Eq. (42).

$$\begin{bmatrix} (m_1+m_3)s^2+c_1s+k_1 & -k_1 \\ -k_1 & m_2s^2+c_2s+k_2 \end{bmatrix} \times \begin{bmatrix} X_{1,t}(s) \\ X_{2,t}(s) \end{bmatrix} = \begin{bmatrix} D_1(s) \\ D_2(s) \end{bmatrix}$$

$$(42)$$

In this way, the model with uncertainty can accurately capture the dynamic behavior of the floating buoy and the oscillator. By incorporating perturbation terms, the model clarifies the effects of waves and other random factors, leading to a more comprehensive synthesis of the kinematic characteristics of the buoy and oscillator. Consequently, the model is capable of reflecting the dynamic response behavior of the floating buoy and oscillator more accurately in complex environments. Moreover, a hybrid robust control strategy is introduced to enhance the adaptability of the model under complex sea conditions, significantly improving the model stability.

The existence of optimal damping has been confirmed by numerous previous studies. When a resonant pendulum is subject to damping effects, its orbit shifts to a period-1 rotation, which can be described by a linear positive correlation between energy output and the damper coefficient. However, excessive damping can disturb this balance, leading to small-amplitude oscillations. Therefore, determining the optimal damping coefficient is crucial. For scenarios with stable natural conditions, a fixed damper coefficient is simple

to apply. However, to accommodate more diverse scenarios, a dynamic damper coefficient strategy is commonly utilized, meaning that the optimal damper coefficient is not unique when modeling the energy output of the WEC.

To address the challenges posed by complex sea states and unpredictable factors, a dynamic damper coefficient is deployed. The dynamic damper coefficient influenced by stochastic interference is modeled as a time-dependent random variable, denoted as c(t). Its stochastic interference term is represented as $\Delta c(t)$, accounting for changes in unpredictable environmental conditions and the operational state of the proposed WEC. Thus, c(t) is expressed as $c(t) = c_0 + \Delta c(t)$, where c_0 is the baseline resistance coefficient. We assume that the stochastic interference term follows a normal distribution $\Delta c(t) \sim \mathcal{N}(0, \sigma_c^2)$. Regarding the output power caused by wave forces applied to the floating buoy, denoted as P_f , the velocity of the buoy $v_{b,t}$ is obtained by differentiating the buoy's position $v_{b,t} = dx_{b,t}/dt$. Furthermore, the wave force $F_{\rm w}$, derived from the kinetic equation, is used to represent the applied wave force, as described in Eq. (43). The resistance coefficient is denoted as $c_{\rm h}$. In this context, the randomized interference term is $\Delta c(t)$ rather than $D_{\rm u}$. The wave force applied to the floating buoy is defined as

$$F_{\rm w} = f\cos(\omega t) - (c_0 + \Delta c(t))\frac{\mathrm{d}x_{b,t}}{\mathrm{d}t} + D_1 \tag{43}$$

Similarly, let P_v denote the wave power of the vibrator, with the corresponding velocity represented as $v_{v,t}$. The spring force F_s is given by

$$F_{s} = k_{s}(x_{v,t} - x_{b,t}) - (c_{v} + \Delta c(t)) \left(\frac{\mathrm{d}x_{v,t}}{\mathrm{d}t} - \frac{\mathrm{d}x_{b,t}}{\mathrm{d}t}\right) \tag{44}$$

where $x_{b,t}$ and $x_{v,t}$ denote the displacements of the floating buoy and the vibrator, respectively. The parameters k_s and c_v represent the stiffness and resistance coefficients of the vibrator.

Thus, the output power P_0 is the sum of P_f and P_v . The power-force relationship is clarified as

$$\begin{cases} P_{f} = F_{w} \cdot v_{b,t} = \\ \left[f \cos(\omega t) - (c_{0} + \Delta c(t)) \frac{dx_{b,t}}{dt} + D_{1} \right] \cdot \frac{dx_{b,t}}{dt}, \\ P_{v} = F_{s} \cdot v_{v,t} = \\ \left[k_{s}(x_{v,t} - x_{b,t}) - (c_{v} + \Delta c(t)) \left(\frac{dx_{v,t}}{dt} - \frac{dx_{b,t}}{dt} \right) \right] \cdot \frac{dx_{v,t}}{dt} \end{cases}$$

$$(45)$$

Then, the total output power P_0 can be expressed as

$$P_{o} = P_{f} + P_{v} =$$

$$\left[f \cos(\omega t) - (c_{0} + \Delta c(t)) \frac{\mathrm{d}x_{b,t}}{\mathrm{d}t} + D_{1} \right] \cdot \frac{\mathrm{d}x_{b,t}}{\mathrm{d}t} +$$

$$\left[k_{s}(x_{v,t} - x_{b,t}) - (c_{v} + \Delta c(t)) \left(\frac{\mathrm{d}x_{v,t}}{\mathrm{d}t} - \frac{\mathrm{d}x_{b,t}}{\mathrm{d}t} \right) \right] \cdot \frac{\mathrm{d}x_{v,t}}{\mathrm{d}t}$$

$$(46)$$

Therefore, we establish the mathematical model concerning the output energy of WEC. The highlight of our proposed formulation is the inclusion of uncertainty instead of single energy output calculation, as well as the chronological complexity is considered, which makes our model more grounded. As for the case of fixed coefficient, it can be regarded as a special situation of the dynamic damper coefficient strategy. What needed to the deployment of the model is to replace the corresponding parameters by constant.

When maximizing the power generated by the WEC,

systematic fatigue that may damage the system must also be considered [32]. Therefore, optimizing systematic damage is a worthwhile endeavor. The friction coefficient is given as $\mu = 0.01$, with the force on the floating buoy in the perpendicular direction denoted as N. The motion velocity of the buoy is represented as $|v_b(t)|$. Consequently, the damage caused by the friction between the water surface and the WEC is expressed as $\int_0^{t_f} \mu \cdot N \cdot |v_b(t)| dt$. For systematic fatigue damage caused by material loading, its coefficient is initially set as $C_f = 0.003 \text{ N/m}^2$, and it is related to the rate of change of position over time $dx_b(t)/dt$. Thus, this type of damage is expressed as $\int_0^{t_f} C_f \cdot \left(\frac{dx_b(t)}{dt}\right)^2 dt$. Let $C_d = 0.005 \text{ N/m}^4$ be the original dynamic damage coefficient. The acceleration of the WEC is denoted as $d^2x_b(t)/dt^2$. The dynamic equipment damage due to acceleration changes is expressed as $\int_0^{t_{\rm f}} C_{\rm d} \cdot \left(\frac{{\rm d}^2 x_{\rm b}(t)}{{\rm d}t^2}\right)^2 {\rm d}t$. The damage caused by the ebb and flow energy response is considered in this term. Since ocean waves are highly volatile, damage caused by environmental elements is inevitable. With C_h representing the coefficient of damage caused by waves and h(t) representing wave heights, the damage caused by wave environments is defined as $\int_0^{t_{\rm f}} C_{\rm h} \cdot h(t)^2 dt$, where the initial value of $C_{\rm h}$ is 0.002 N/m². Similarly, the influence of wave shocks is accounted by the term $\int_0^{t_{\rm f}} C_{\rm j} \cdot |v_{\rm b}(t)|^3 {\rm d}t$, where $C_{\rm j}$ is the damage coefficient related to shock effects, with an initial value of 0.04 N/m³. Thermodynamic damage due to comprehensive effects, such as friction and material deformation, is considered in the term $\int_0^{t_f} C_t \cdot T(t)^2 dt$, where the thermodynamic damage coefficient is initially set as $C_t = 0.001 \text{ N/m}^2$, and T(t) represents the absolute temperature of the floating buoy. As long as friction and resistance exist, thermodynamic damage may occur. Finally, damage because of a combination of other environmental factors, such as salinity, wind speed, and similar influences, is defined as $\int_0^{t_f} C_e \cdot E(t) dt$, where E(t)represents the wave band energy density associated with environmental factors, and the corresponding coefficient is given as $C_{\rm e} = 0.01 \text{ N/m}^{3}$.

Overall, the systematic damage of the WEC is denoted as *D* and is expressed as

$$D = \int_{0}^{t_{\rm f}} \left(\mu \cdot N \cdot |v_{\rm b}(t)| + C_{\rm f} \cdot \left(\frac{\mathrm{d}x_{\rm b}(t)}{\mathrm{d}t} \right)^{2} + C_{\rm d} \cdot \left(\frac{\mathrm{d}^{2}x_{\rm b}(t)}{\mathrm{d}t^{2}} \right)^{2} + C_{\rm h} \cdot h(t)^{2} + C_{\rm j} \cdot |v_{\rm b}(t)|^{3} + C_{\rm t} \cdot T(t)^{2} + C_{\rm e} \cdot E(t) \right) \mathrm{d}t$$

$$(47)$$

By establishing a model describing the damage of the WEC in power generation, nonlinear and unpredictable factors in complex systems concerning the WEC and the working conditions that impact systematic damage are considered. This

proposed multi-dimensional model provides a comprehensive framework for damage analysis and evaluation.

B. Cost Function

Our aim is the simultaneous maximization of the output energy and minimization of accumulated damage caused by the work of WEC and the unforeseeable incidents in the environment. In the establishment of model, the formulations of output power and systematic damage are constructed. Because of to the requirements of dual-objective optimization, the transformation from the systematic physical performance to the mathematical problem is crucial to realize our optimization objectives [36].

Let J_1 be the cost function concerning the maximum of the output energy P_0 . Define C_d as the damage coefficient related to the velocity of the buoy, and C_s as that of the vibrator. These two coefficients quantify the damage caused to both the buoy and the vibrator. C_d and C_s correspond to the damage weights of the buoy and vibrator's velocity squared terms, respectively, and are equivalent to the viscous damping coefficients (N·s/m). To account for extra energy loss that captures mechanical damage and fatigue, this study introduces $C_{\rm u}$ as the damage coefficient caused by input power. Moreover, the output power is represented as $-\int_0^{t_f} P_o(t) dt$. Where taking a negative value is convenient for maximizing the output energy. Define u(t) as an adjustable variable representing the controllable energy applied from external sources, with t_f denoting the end time of the WEC operation. These parameters change dynamically in real-time. Herein, $C_{\rm u}$ measures the additional mechanical wear caused by external control input. Since the u(t) is measured in N, the unit of C_u is J/N^2 .

The device reacts differently to the external environment at different times. Damage to equipment is superimposed over time, and its marginal rate of damage continues to change over time of use. Therefore, when analyzing the relationship between WEC damage and its operational time, a time decay factor $e^{-\lambda t}$ is introduced in J_1 . Here, λ is the velocity rate constant of $e^{-\lambda t}$ with the unit of s^{-1} , primarily representing the incremental rate of equipment damage over time. Consequently, the term considering damage due to kinetic factors in J_1 with the time decay factor is expressed as

$$\int_0^{t_{\rm f}} \left(C_{\rm d} \mathrm{e}^{-\lambda t} \left(\frac{\mathrm{d} x_{\mathrm{b},t}}{\mathrm{d} t} \right)^2 + C_{\mathrm{s}} \mathrm{e}^{-\lambda t} \left(\frac{\mathrm{d} x_{\mathrm{v},t}}{\mathrm{d} t} \right)^2 + C_{\mathrm{u}} \mathrm{e}^{-\lambda t} u(t)^2 \right) \mathrm{d} t.$$

Furthermore, a feedback term for systematic states is incorporated to provide a comprehensive assessment of operational states and working conditions. Define a state variable function $h\left(x_b(t), x_v(t), u(t), \frac{\mathrm{d}x_{b,t}}{\mathrm{d}t}, \frac{\mathrm{d}x_{v,t}}{\mathrm{d}t}\right)$, which captures the intricate correlation of matching status changing over time, including $x_b(t)$, $x_v(t)$, and u(t). To quantify variations, we define h_1 and h_2 . Wherein, h_1 expresses the squared velocity difference (e.g., velocity mismatch) and h_2 represents the loss induced by input power.

Thus, Eq. (48) describes more complex relationships in the system, incorporating multicollinearity effects among variables.

$$h\left(x_{b}(t), x_{v}(t), u(t), \frac{\mathrm{d}x_{b,t}}{\mathrm{d}t}, \frac{\mathrm{d}x_{v,t}}{\mathrm{d}t}\right) = h_{1}\left(\frac{\mathrm{d}x_{b,t}}{\mathrm{d}t}, \frac{\mathrm{d}x_{v,t}}{\mathrm{d}t}\right) + h_{2}(u(t))$$
(48)

Finally, the gap between the velocity of the buoy v_b and the vibrator v_v is measured using two weight coefficients α and β . Here, α serves as an operational variable to control the impact caused by different changes in state variables and input, while β regulates the influence on overall damage caused by input energy, expressed as

$$\sqrt{\left(\frac{\mathrm{d}x_{\mathrm{b},t}}{\mathrm{d}t} - \frac{\mathrm{d}x_{\mathrm{v},t}}{\mathrm{d}t}\right)^2 + \beta(u(t))^2} \mathrm{d}t. \quad \text{In specific, } \alpha \quad \text{controls the weight given to the thermal-mechanical coupling damage because of the mechanism's kinematic mismatch, and } \beta \quad \text{balances the relative contributions of the velocity difference and control force components of the mismatch term, which are controllable variables.}$$

Hence, J_1 can be formulated as Eq. (49), integrating the three aforementioned terms.

$$\max_{s.t., \text{ min } J_{1}(x(t), u(t), t_{f}) = -\int_{0}^{t_{f}} \left[\left(f \cos(\omega t) - (c_{0} + \Delta c(t)) \right) \frac{dx_{b,t}}{dt} + D_{1} \right) \frac{dx_{b,t}}{dt} + \left(k_{s}(x_{v,t} - x_{b,t}) - (c_{v} + \Delta c(t)) \left(\frac{dx_{v,t}}{dt} - \frac{dx_{b,t}}{dt} \right) \right) \frac{dx_{v,t}}{dt} \right] dt + (49)$$

$$\int_{0}^{t_{f}} \left[C_{d} e^{-\lambda t} \left(\frac{dx_{b,t}}{dt} \right)^{2} + C_{s} e^{-\lambda t} \left(\frac{dx_{v,t}}{dt} \right)^{2} + C_{u} e^{-\lambda t} u(t)^{2} \right] dt +$$

$$\alpha \int_{0}^{t_{f}} \sqrt{\left(\frac{dx_{b,t}}{dt} - \frac{dx_{v,t}}{dt} \right)^{2} + \beta(u(t))^{2}} dt$$

Generally speaking, J_1 encapsulates both the description of power output and systematic state feedback. This paper integrates output power and seeks to maximize energy output. Additionally, a more comprehensive formulation of the cost function accounts for discrepancies in the velocity of the buoy and vibrator, based on the squared-root method. The influence of input energy is also considered through this approach.

In the construction of the cost function of systematic damage J_2 , two terms L and $\beta \int_0^{t_{\rm f}} \max\{C_{\rm u} u(t)^2 + C_{\rm h} h(t)^2, 0\} \mathrm{d}t$ are considered as the dynamic damage and the quadratic form of extra systematic damage, respectively. The term of damage L is caused by motion. In these two formulations, α and β serve as normalizing factors for making the corresponding terms dimensionless.

For the damage because of the velocity x_b , the corresponding term in the cost function is $C_f \cdot \left(\frac{\mathrm{d}x_{b,t}}{\mathrm{d}t}\right)^2$. Similarly, the damage caused by x_v is $C_d \cdot \left(\frac{\mathrm{d}x_{v,t}}{\mathrm{d}t}\right)^2$. For a

coefficient of input u(t), which causes damage $C_{\rm u}$, a term $C_{\rm u}(u(t))^2$ is introduced to quantify this item of damage. The coefficient of systematic damage related to the velocity difference in the relative displacement of the buoy and vibrator is defined as $C_{\rm r}$. This type of damage is given as

 $C_{\rm r} \left(\frac{{\rm d}x_{{\rm v},t}}{{\rm d}t} - \frac{{\rm d}x_{{\rm b},t}}{{\rm d}t}\right)^2$. $C_{\rm r}$ is used to penalize the structural shear stresses generated by the relative velocity of the float-vibrator $(v_{\rm v} - v_{\rm b})^2$ in the same units as $C_{\rm d}$.

Then, integrating the term accounting for damage because of wave height and the acceleration of the buoy into dynamic damage, the term L is finally obtained. Considering the nonlinear relationships between the damage and input, the damage is proportional to the square of the input. The expression $C_{\rm u}u(t)^2 + C_{\rm h}h(t)^2$ represents the damage cost function concerning the association between input u(t) and wave height h(t). Thus, the cost function of systematic damage J_2 is defined as

$$J_2(x(t), u(t), t_f) = L + \beta \int_0^{t_f} \max\{C_u u(t)^2 + C_h h(t)^2, 0\} dt$$
 (50)

$$L = \alpha \int_{0}^{t_{f}} \left[C_{f} \left(\frac{\mathrm{d}x_{b,t}}{\mathrm{d}t} \right)^{2} + C_{d} \left(\frac{\mathrm{d}x_{v,t}}{\mathrm{d}t} \right)^{2} + C_{u}(u(t))^{2} + C_{r} \left(\frac{\mathrm{d}x_{v,t}}{\mathrm{d}t} - \frac{\mathrm{d}x_{b,t}}{\mathrm{d}t} \right)^{2} + C_{h}h(t)^{2} + C_{j} \left| \frac{\mathrm{d}^{2}x_{b,t}}{\mathrm{d}t^{2}} \right|^{2} \right] \mathrm{d}t$$
(51)

Consequently, the cost function J_2 serves as a comprehensive evaluation metric for predicting the systematic damage of the proposed WEC, considering multiple influencing factors under diverse scenarios.

IV. METHODOLOGY

A. Runge-Kutta Method

Because of the numerous parameters required for solving the WEC model under volatile working conditions, a simple direct solution is not feasible. Therefore, the RK-4 method is chosen for its simplified solution approach. The RK method, which can be implemented through software simulations, avoids the complexity of manual solving. This method is an iterative technique for solving nonlinear ordinary differential equations, offering high accuracy by using the Taylor's formula and slope approximations instead of differentiation. Essentially, the fourth-order Runge-Kutta method enhances accuracy by calculating multiple slopes per step. We use the dynamic damper coefficient as an example for demonstrating the solution process.

We set h and t_n as the step size and time, respectively, as well as the time value t_{n+1} as the sum of t_n and h. Besides, y_n is the value in time t_n , which also represents the target function. Then the first slope k_1 is calculated as Eq. (52), which expresses the change rate in point (t_n, y_n) .

$$k_1 = h f(t_n, v_n) \tag{52}$$

Thus, the second slope k_2 is the y_n predicted based on k_1 in the place of $t_n + h/2$, as shown in Eq. (53).

$$k_2 = hf\left(t_n + \frac{h}{2}, y_n + \frac{k_1}{2}\right)$$
 (53)

Therefore, the third slope k_3 is calculated based on Eq. (54).

$$k_3 = hf\left(t_n + \frac{h}{2}, y_n + \frac{k_2}{2}\right)$$
 (54)

Finally, the slope calculation is completed based on the fourth slope k_4 , as defined in Eq. (55).

$$k_4 = h f(t_n + h, y_n + k_3)$$
 (55)

Derived from the calculation of slope, y_n is updated to calculate y_{n+1} . This process is described in Eq. (56). It is obvious that values after the updated step, according to weights, reflect more accurate dynamic changes. Repeating the above process, iterating until the end time is reached, the result is obtained.

$$y_{n+1} = y_n + \frac{1}{6}(k_1 + 2k_2 + 2k_3 + k_4)$$
 (56)

The dynamical equations about the floating buoy and the vibrator have already been established in the problem formulation to form the coupled second-order differential equations, which take into account the motion of the floating buoy under the action of waves, including the hydrostatic restoring force, additional inertia force, the hinged-wave damping force, etc. Moreover, uncertainty terms are simultaneously included. Based on the above model, the solutions of the motion models of the floating buoy and oscillator are obtained according to the RK-4 method. Specifically, the method is utilized to transform the secondorder differential equations into the first-order differential equations for solution, and iterative solving is carried out to compute the complete data of the displacement and velocity of the floating buoy and vibrator under the influence of waves with respect to time.

Because of the classic RK method normally being applied to solve the first-order differential equations, we convert the second-order differential equations to first-order by introducing new variables for obtaining a solution. Let new variables be defined as u_1 , u_2 , w_1 , w_2 , p_1 , p_2 , q_1 , and q_2 , thus the definition in Eq. (57) is set. The $u_1 = x_{1,r}$ in the first term is the motion of the buoy, and the $u_2 = dx_{1,r}/dt$ represents the velocity. The second term concerning w_1 and w_2 corresponds to the motion and velocity of the vibrator, respectively. The third and fourth terms denote the angular displacement and velocity, corresponding to the buoy and vibrator.

$$\begin{cases} u_{1} = x_{1,t}, \ u_{2} = \frac{\mathrm{d}x_{1,t}}{\mathrm{d}t}; \\ w_{1} = x_{2,t}, \ w_{2} = \frac{\mathrm{d}x_{2,t}}{\mathrm{d}t}; \\ p_{1} = \theta_{1}, \ p_{2} = \frac{\mathrm{d}\theta_{1}}{\mathrm{d}t}; \\ q_{1} = \theta_{2}, \ q_{2} = \frac{\mathrm{d}\theta_{2}}{\mathrm{d}t} \end{cases}$$
(57)

Thus, a system of differential equations with reduced order is obtained to facilitate subsequent calculations.

In our study, traditional Runge-Kutta methods are limited in accuracy and adaptability in numerical solving due to the fixed step size and order. Therefore, it is difficult for RK method to capture the high-frequency, nonlinear fluctuations in volatile sea states for volatile changes may be skipped. Therefore, we propose the dynamic order adaptive Runge-

Kutta method, which dynamically adjusts both the step size and the integration order in response to local truncation error. This adaptive mechanism enables finer resolution during abrupt wave changing to preserve numerical stability, while coarsening the step in stable conditions to improve computational efficiency.

To be specific, let a controllable variable be defined as Δt , and denote ζ as the corresponding allowed error threshold. The parameter p represents the order of the numerical method, thus the new step size Δt_{new} is defined in Eq. (58), where the error is acquired based on the comparison between the calculated high-order method y_{h} and the low-order method y_{l} : error = $|y_{\text{h}} - y_{\text{l}}|$.

$$\Delta t_{\text{new}} = \Delta t \times \left(\frac{\zeta}{\text{error}}\right)^{\frac{1}{p+1}}$$
 (58)

Comparing the error with ζ , the step size h is decreased when error $> \zeta$, which is noted as $h \leftarrow \beta h$, $\beta < 1$. Conversely, to increase the value of h, we define $h \leftarrow \gamma h$, $\gamma > 1$. For instance, if the step size calculated by RK-4 results in excessively large error, a smaller step size shall be selected. The mechanism functions similarly in the opposite scenario. This is the core mechanism for dynamic order selection.

For implementation, the initial conditions t_0 and y_0 , original step size h, and error threshold ζ are set. The calculation is then performed using the classic RK-4 and RK-5 methods. After obtaining error, the step size h and order p are adjusted accordingly. Finally, the state variable (t_n, y_n) is calculated after iterations until the end time t_f is reached.

Thus, our proposed DOARK method achieves a more robust balance between accuracy and computational efficiency by introducing a dual adaptation mechanism, which dynamically adjusts both integration step size and order. Although the adaptive Runge-Kutta methods have already been developed. this method relies solely on local truncation error for step control and uses a fixed order. However, our proposed DOARK incorporates environmental volatility as an additional feedback signal, enabling context-aware adaptation. This is particularly advantageous in wave energy systems, where real-time wave conditions are inherently uncertain and highly non-stationary. Under volatile sea states, DOARK increases resolution through reduced step sizes and higherorder integration, thereby suppressing transient errors and preserving numerical stability. Conversely, during stable periods, it coarsens the integration to avoid redundant computation, thus improving efficiency. As a result, DOARK not only reduces global error accumulation but also better supports the coupled control-dynamic system, making it more suitable than classical RK methods for uncertainty-driven and feedback-sensitive systems, such as WECs.

Unlike traditional adaptive Runge-Kutta methods that rely solely on local truncation error and fixed integration order, such as Runge-Kutta-Fehlberg-45 (RKF-45), which adjusts only the step size based on local error estimations. DOARK introduces a dual-adaptation mechanism that adjusts both step size and integration order in real time. This enables it to better capture fast-changing system dynamics and nonlinear

stiffness. Moreover, DOARK integrates environmental volatility as an additional input signal for solver adjustment, allowing the algorithm to respond contextually to transient disturbances. This enhances its sensitivity to abrupt kinetic transitions and significantly improves numerical robustness and resolution accuracy in wave-dominated and uncertainty-prone systems.

B. Adaptive Step Size Search

To calculate the maximum output power of the device, the optimum damping coefficient must be determined. When the damping coefficient is fixed, an adaptive step size searching algorithm is employed to solve the single-parameter optimization equation. This involves setting the damping coefficient range and initial step size, then iterating over the range and calculating the average output power for each damping coefficient. The step size is adjusted based on the solved interval, with larger step sizes for wider intervals and smaller ones as the interval narrows. For dynamic coefficients, the damping is proportional to the exponentiation of the relative velocities between the floating body and the vibrator, with a range for both proportionality and exponentiation. In this case, a dual parameter optimization is required for both damping and scaling coefficients. A double loop is used to explore all possible combinations, and for each, the average output power is calculated using the Runge-Kutta method along with the adaptive step size strategy. The combination yielding the highest output power is selected. The proportionality is ranged from 0 to 100,000 while the range of exponentiation is (0,1). For finer optimization, the optimal damping coefficients for both linear and rotary dampers are considered. We observe that when the damping coefficient is between 95,000 and 10,000, and the power index is between 0.4 and 0.5, the optimal power change rate is minimal, suggesting that the adaptive step size algorithm may not provide the desired accuracy. Thus, the simulated annealing algorithm is a more suitable method for this case.

C. Multi-Objective Optimization

As the WEC model is enhanced and a more accurate output energy is calculated with DOARK, multi-objective optimization for energy generation and equipment damage shall be conducted. Multi-objective optimization refers to mathematical optimization problems that involve the optimization of multiple objective functions simultaneously. In this work, the maximum output power P_0 and the minimum systematic damage D are considered synchronously as two objective functions. In multi-objective optimization, a dynamic balance between objectives with diverse characteristics must be achieved [37]. Commonly, multiple objectives may even conflict with each other.

Hence, the multi-objective constraint method, which converts multi-objective problems into single-objective optimization problems, is a reasonable approach. Specifically, we select one objective as the primary objective function, while the other is used as a constraint condition. Herein, the primary objective is to maximize $P_{\rm o}$, while minimizing D is designed as a constraint.

For systematic damage D, it must be constrained within the tolerance range $D_{\rm max}$ to ensure the long-term stability and reliability of the WEC system. Based on the selection of the primary objective and constraints, we establish the following optimization problem.

$$\min P_{o},$$
s.t., $D \le D_{\text{max}}$ (59)

Thus, output power is enhanced as much as possible while ensuring that systematic damage remains within the tolerance range to balance the trade-off between power output and damage.

Since the physical characteristics of P_0 and D are difficult to optimize on the same scale because of computational challenges, a transformation is required. Therefore, mathematical analysis and strategic support are taken into account, leading to the conversion of P_0 and D into cost functions J_1 and J_2 , respectively. The objective is to minimize both J_1 and J_2 under the given constraints, i.e., $\min(J_1,J_2)$.

However, multi-objective optimization problems generally do not have a unique solution, as multiple Pareto-optimal solutions exist. To resolve conflicts between objectives and determine Pareto-optimal solutions, the general form of a multi-objective problem is given in Formula (60).

min
$$\{J_1, J_2, ..., J_k\}$$
,
s.t., $x \in Z$ (60)

where $\{J_1, J_2, ..., J_k\}$ are the objective functions, x represents the set of decision variables, and Z denotes a set of constraints [34].

We utilize the ε -constraint method to solve the multiobjective problem. Its principal idea is to select one objective function as the primary optimization target, while treating the other objective functions as constraints [38, 39]. This reformulates the multi-objective optimization problem as Formula (61).

min
$$J_1$$
,
s.t., $J_2 \ge \varepsilon_2$,
 $J_3 \ge \varepsilon_3$,
 \vdots
 $J_k \ge \varepsilon_k$,
 $x \in Z$ (61)

Based on the application of the ε -constraint method, one of the objectives is treated as the main parameter, while the remaining k-1 objectives are considered constraints. We select the maximum power output P_0 as the primary objective, while the minimum systematic damage D is constrained. Hence, the Pareto set is obtained for the multi-objective problem by finding a suitable parameter ε . For this reason, we adopt a fuzzy-based decision-making approach to identify the leading solution from the Pareto set. The set in (0,1) represents alternative solutions [39]. The fuzzy membership function for objective \hat{J}_k is defined as Eq. (62).

$$\hat{J}_{k} = \begin{cases} 1, J_{k} \leq J_{k}^{\text{Low}}; \\ \frac{J_{k}^{\text{max}} - J_{k}}{J_{k}^{\text{max}} - J_{k}^{\text{min}}}, J_{k}^{\text{Low}} \leq J_{k} \leq J_{k}^{\text{Up}}; \\ 0, J_{k} \geq J_{k}^{\text{Up}} \end{cases}$$
(62)

where \hat{J}_k denotes the normalized objective function, with its minimum and maximum limits given by J_k^{\min} and J_k^{\max} , respectively.

To determine the optimal solution, the mix-min technique is applied to select the best solution from the Pareto set, as described in Eq. (63).

Solution =
$$\max \left\{ \min \begin{bmatrix} \hat{J}_1 \\ \hat{J}_2 \\ \vdots \\ \hat{J}_k \end{bmatrix} \right\}$$
 (63)

We conduct dual-objective optimization by simulation in three different scenarios. The uncertainty of unstable water region has been considered in the multi-objective problem. To do so, Monte-Carlo simulation is used to generate 1000 scenarios. We select the three representative scenarios that are corresponding to stable sea condition, normal sea condition, and volatile sea condition, respectively. The wave data are constructed based on a database collected by US Water Power Technologies Office integrated with Ref. [40]. Meanwhile, wave conditions collected in our laboratories are also included in this database. Thus, a custom database is constructed for simulation. Our data contain wave conditions of more than 40,000 time points. We perform the filtration for the database to select data to construct the three different scenarios in the process of simulation. Most of the characteristics are based on the west coast of America. Our analysis is based on a wide range of sea state scenarios including stable, normal, and volatile conditions of the classic study case. Combined with Monte-Carlo simulations, the generalization is proven rather than improvements in specific or idealized conditions.

We rank the original observation by the composite intensity $S(t) = ||[h(t), P_{w}(t), V_{g}(t)]||_{2}$, corresponding to instantaneous wave height, theoretical wave power density, and gust speed, respectively. Wherein, 3 percentiles are defined as scenarios I-III, corresponding to stable, normal, and volatile marine conditions. More than 200 consecutive 100 s clips are extracted from each segment, and the first four peaks are extracted by fast Fourier transform (FFT) for each of them. Then, the first peak amplitude A_1 and frequency ω_1 are injected into the model external excitation $f\cos\omega t$, the remaining three peaks are assigned to the perturbation term D_1 – D_4 , and the standard deviation of the residuals σ is given as Gaussian noise $D_{\rm u}$. Then, we schedule the adaptive damper via $c(t) = c_0 + kP_w(t)$ with k tuned under the damage cap. Each scenario undergoes 1000 Monte-Carlo runs in the DOARK solver to quantify power yield and safety margin.

After then, the multi-objective problem is solved by ε -constraint as the best comprise acquired by this method. To find the optimal Pareto compromise, we utilize the fuzzy membership function, as our early research [39].

V. EXPERIMENT

A. Comparison Analysis of the Optimized Model

To prove the utilization of our proposed model with uncertainty, we compare the performance of original model with the model with uncertainty. As the accuracy of the model with uncertainty verified, the traditional RK-4 and the DOARK are applied respectively, whose performances are then compared. We compare the simulated results with the ground truth collected in real experimental field for proving the performance.

The numerical implementations are performed with Python and the PyDSTool package is utilized for simulation and calculation. PyDSTool is an efficient tool based on the Python to obtain the solution for dynamic system, which is significant in solving differential equations in particular [41]. Besides, the scipy.signal is utilized for frequency domain analysis. Additionally, PyFOAM, which is a Python tool based on OpenFOAM, is also involved in sea conditions. After determining the input parameters and data, the Monte-Carlo simulation is used to generate abundant scenario about the work condition of WEC for obtaining the optimal value of physical coefficient. The marine conditions manufactured in our grounded platform are also referred by the simulation system in computer. Moreover, the CPU utilized for experiment is the 13th Gen Intel(R) Core(TM) i7-13650HX 2.60 GHz and the RAM of our experimental platform is 16.0 GB. The simulated annealing algorithm is a stochastic optimization search algorithm based on an iterative solution strategy.

Some critical parameters not explicitly mentioned but essential for the simulation setup are listed in Table 1.

Key parameters such as buoy mass, bottom radius, cylindrical, conical part heights, etc., serve as fundamental inputs. Additionally, derived quantities, including the volume of the buoy's cylindrical and conical sections, as well as the draft and initial equilibrium position of the vibrating component, are determined based on the classical physical principles. To investigate different dynamic scenarios, two cases are considered in the simulation. In case 1, the damping coefficient remains fixed, whereas in case 2, it is dynamically adjusted. Furthermore, the optimal initial values of critical physical coefficients, such as $C_{\rm f}$ and $C_{\rm d}$, are obtained through the simulation process.

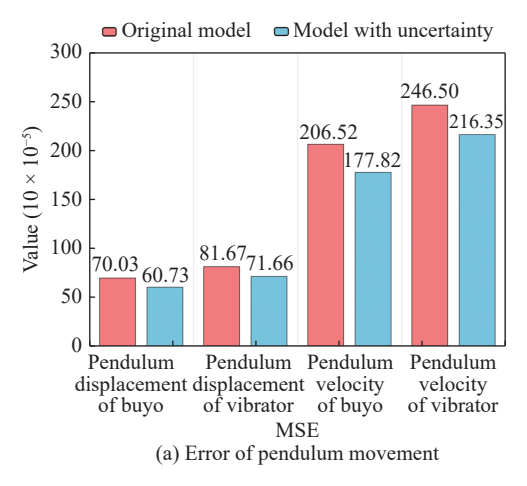
The comparison between the errors of calculated kinetic characteristics under the wave conditions given in our ground experimental platform of the original model and the model with uncertainty is depicted in Fig. 3. The errors are measured by the mean square error (MSE) between the calculated values and the ground truth. It is obvious that our proposed model with uncertainty has overwhelming advantages in calculating the kinetic characteristics of the WEC. For instance, in the case of the pendulum velocity of the vibrator, the introduction of uncertainty makes the error decrease from 246.50 to 216.35, achieving a reduction magnitude of 30. The results suggest that the model is optimized in terms of the accuracy of kinetic characteristic calculations for our proposed system. Particularly, for parameters related to velocity, the

Table 1 Setting parameter for testing.

Specification	Parameter
Buoy mass	4866 kg
Buoy bottom radius	1 m
Buoy cylindrical part height	3 m
Buoy conical part height	0.8 m
Volume of buoy cylindrical part	9.42 m^3
Volume of buoy conical part height	0.83 m^3
Draft of buoy conical part height	2 m
Vibrating mass	2433 kg
Vibrating radius	0.5 m
Vibrating height	0.5 m
Seawater density	$1025\;kg/m^3$
Gravitational acceleration	9.3 m/s^2
Spring stiffness	80,000 N/m
Spring length	0.5 m
Initial spring compression	0.298 m
Rotational spring stiffness	250,000 N·m
Static hydrostatic recovery stiffness coefficient	8890.8 N·m
Initial linear damping coefficient	10,000
Range of damping coefficient	[0, 100,000]

improvements are significantly more pronounced. In summary, the consideration of uncertainty makes the model more accurate when describing the system's kinetic characteristics, as more interference from unpredictable factors in the ground experiment is quantified by the aforementioned established index.

Both of the two models are solved with the conventional forth-order RK method and the output power within 100 s is calculated. The comparison analysis of the proposed optimization model obtained is depicted in Fig. 4. Comparing the performance of the original model with that of the model with uncertainty under case 1 and case 2, the model with uncertainty shows significant advantages in fitting accuracy, error distribution, and stability. Specifically, the model with uncertainty's calculated power output matches the ground truth significantly, especially in the peak power stage e.g., 0-20 s, where the numeric results of peak, amplitude, and distribution trend accurately reflect the power change characteristics of the actual wave energy device whereas the original model shows obvious deviations in this stage, which are manifested in the peak prediction of the peaks with more unacceptable miscalculations. In the perspective of error distribution, the model with uncertainty prevails with a smaller error amplitude and a more uniform distribution comparing with original model, especially in the peak stage of drastic power changes. Meanwhile, the prediction results of model with uncertainty are superior in robustness. In contrast, the original model has significant error fluctuations in the peak stage while the unstable prediction results indicate its lack of stability and accuracy. In addition, the model with uncertainty is more prominent in the physical meaning, which can more accurately capture the dynamic power output



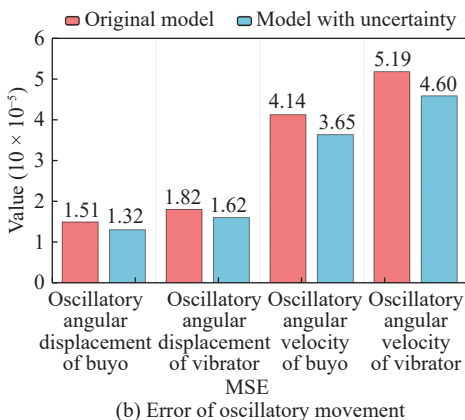


Figure 3 Demonstration of errors of the two models' calculated kinetic characteristics.

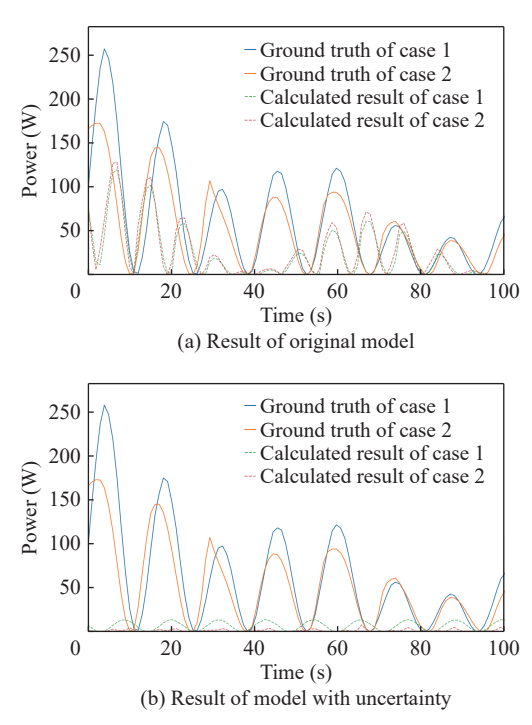


Figure 4 Comparison of two proposed models solved with the conventional fourth-order Runge-Kutta method.

characteristics of wave energy devices and not solely can its prediction results describe the physical characteristic of peak distribution and trend changes, but also provide more scientific data support for the optimal design and performance evaluation of the devices. Generally speaking, it can be referred from Fig. 4 that the proposed model with uncertainty is superior to the original model with a higher accuracy, robustness, and applicability, which provides a more scientific and efficient tool for the modeling of wave energy devices and is an ideal choice for further research simultaneously.

The comparison of error variations between the two models under wave conditions in our ground experimental platform is illustrated in Fig. 5. As shown in Fig. 5(a), regardless of case 1 or case 2, the errors of the original model exhibit larger initial deviations compared with the model with uncertainty. Additionally, the error increases progressively over time, with pronounced oscillations throughout the time series. This suggests that the original model struggles to capture the fluctuation patterns smoothly.

In contrast, as depicted in Fig. 5(b), the introduction of uncertainty significantly reduces the errors within a shorter time span. Specifically, in both case 1 and case 2, the peak errors are mitigated to approximately 50 W, indicating that the model with uncertainty captures the dynamic behavior of the WEC at high power outputs with superior accuracy. As the time series progress, the error magnitude of the uncertainty-integrated model continues to decline, demonstrating a more uniform distribution and eventual convergence toward zero. Compared with the original model, the uncertainty-integrated model exhibits a reduced fluctuation amplitude, particularly in case 2, underscoring its enhanced accuracy and stability under complex fluctuating conditions.

Table 2 presents the total mean squared error of the output power for both models in case 1 and case 2. In case 1, the prediction capabilities of the two models are quantified as

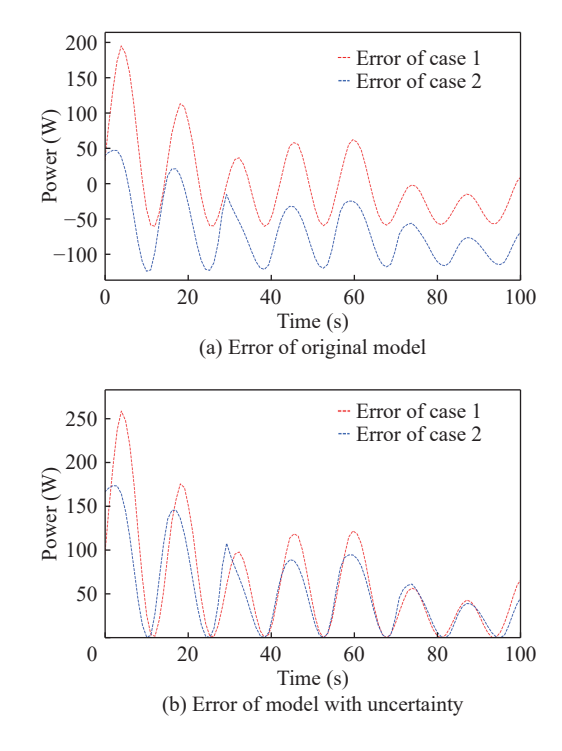


Figure 5 Error changes of the two models within 100 s.

2110.0118 and 2014.1258, respectively. The discrepancy between the two models is minimal, and the optimized model achieving a reduction of 4.54% in MSE. This suggests that under simple conditions, the performance difference between the two models is relatively insignificant. However, under the more complex conditions of case 2, the deviation between the two models becomes significantly larger, with the optimized model achieving a remarkable 74.98% reduction in MSE. The MSE of the uncertainty-integrated model is more than four times lower than that of the original model, demonstrating a substantial improvement in its ability to capture the dynamics of the power output under fluctuating conditions as the dynamic damper coefficient is a common situation.

Table 2 MSE of output power in case 1 and case 2 of original model and model with uncertainty.

Model	MSE in case 1	MSE in case 2
Original model	2110.0118	7038.0788
Model with uncertainty	2014.1258	1761.0898

Generally speaking, in the traditional WEC modeling, system motions are often assumed to be subjected to ideal and high-frequency disturbances, superposition effects, and sudden external perturbations prevalent in the marine environment are neglected. In our study, the ability of the model to fit the nonlinear response behavior under real sea states is enhanced by constructing multiple perturbation terms and introducing nondeterministic disturbance factors into the system dynamics equations. These perturbation terms, formed by time-varying sinusoidal components and Gaussian noise, allow the model to reflect non-stationary dynamic characteristics more accurately. This uncertainty-integrated structure not only improves the realism of input excitation but also enhances the model's sensitivity to transient kinetic changes. As a result, the numerical solver can better track local gradient variations and dynamic transitions, especially in high-energy intervals such as 0-20 s. The dynamic coupling introduced by stochastic terms improves the phase alignment, amplitude fidelity, and stability of output power predictions. Therefore, the model with uncertainty achieves stronger consistency with ground truth data in both steady and volatile sea conditions, providing a more robust foundation for performance evaluation and optimization.

B. Performance Analysis of DOARK

To illustrate the system's behavior, we present the motion responses of the buoy and vibrator. For the initial analysis, we consider the case, in which the WEC undergoes only pendular motion. The displacement and velocity of the buoy and vibrator in the pendular mode are computed, and the corresponding results are depicted in Fig. 6.

When incorporating oscillatory motion, a more realistic scenario, the displacement and velocity of the buoy and vibrator are further computed, building upon the previously obtained pendular motion results. The discrepancies between the computed values and the ground truth are illustrated in

Figs. 7 and 8. Specifically, Fig. 7 presents the simulation results obtained using the RK-4 method, whereas Fig. 8 depicts the corresponding results using DOARK. A comparative analysis reveals that the RK-4 algorithm exhibits a larger error margin and higher oscillation amplitude, particularly evident in the fluctuations of displacement and velocity curves. In contrast, DOARK demonstrates a smoother error profile and is more effective in maintaining a lower cumulative error over extended time steps. This outcome highlights the adaptive step-size adjustment feature of DOARK, which enables it to dynamically fine-tune internal parameters for improved accuracy in complex dynamic systems.

The superiority of DOARK is further substantiated by the error metrics presented in Table 3. When modeling the physical motion of the WEC, DOARK achieves a lower MSE of 61.65, which is approximately 8% lower than that of the RK-4 method. Although both algorithms exhibit higher MSE values when solving oscillatory angular motion compared with pure pendular motion, DOARK consistently outperforms RK-4 across all scenarios. This indicates that while the performance difference between the two algorithms is marginal in single-dimensional simple motions, DOARK demonstrates significant advantages in handling multidimensional dynamic interactions. Consequently, proposed DOARK algorithm is more effective than traditional methods in capturing the complex physical characteristics of WECs, making it a robust tool for accurate motion simulation in marine energy applications.

Based on the computed pendulum displacement, velocity, oscillatory angular displacement, and velocity of the buoy and vibrator, the corresponding output energy is obtained. The DOARK algorithm is applied to solve the model incorporating uncertainty in output energy, with results presented in Figs. 9 and 10.

As shown in Fig. 9, the predicted output progressively converges to the ground truth across the entire 100 s time series. The accuracy of the computed output in case 1 and case 2 demonstrates a notable improvement compared with the results in Fig. 4, indicating that DOARK enhances overall accuracy in handling both simple fixed damping coefficient cases and complex dynamic damping coefficient scenarios.

Furthermore, the MSE of the output energy, computed using DOARK, is approximately 1761.0996 for case 1 and 1596.8001 for case 2, as summarized in Table 4. Compared with the fourth-order Runge-Kutta method, DOARK achieves 12.56% and 9.36% reductions in MSE for case 1 and case 2, respectively. The simulation results exhibit strong agreement with the ground truth, further validating the robustness of the proposed approach.

As illustrated in Fig. 10, the error associated with DOARK exhibits a decreasing trend and stabilizes around 50 s, whereas in Fig. 9, this stabilization occurs at approximately 60 s. This observation suggests that DOARK outperforms the conventional fourth-order Runge-Kutta method in terms of convergence speed, reinforcing its effectiveness in solving complex dynamical systems.

These errors primarily result from the inability of the classical RK method to track sudden dynamic shifts, as it

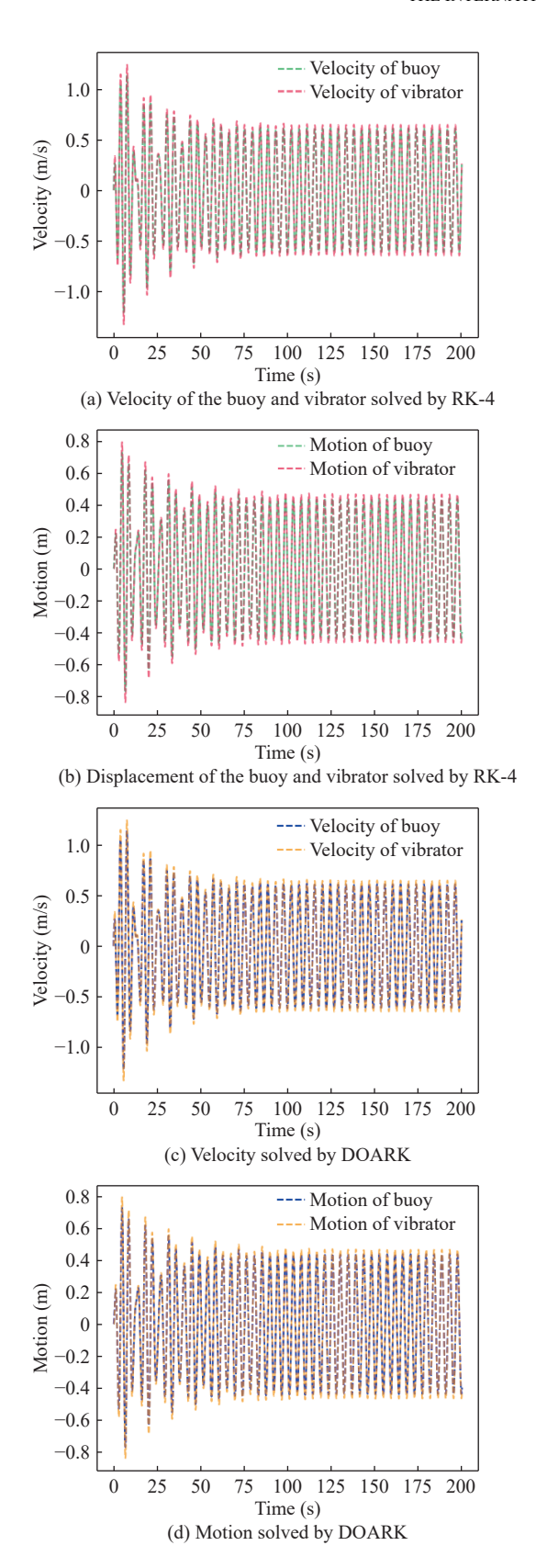


Figure 6 Pendular velocity and displacement of the buoy and vibrator under the case that only pendular motion is considered.

lacks order adaptation and relies solely on error-based step control. Classical adaptive RK methods often exhibit integration lag and underpredict nonlinear oscillations in such conditions.

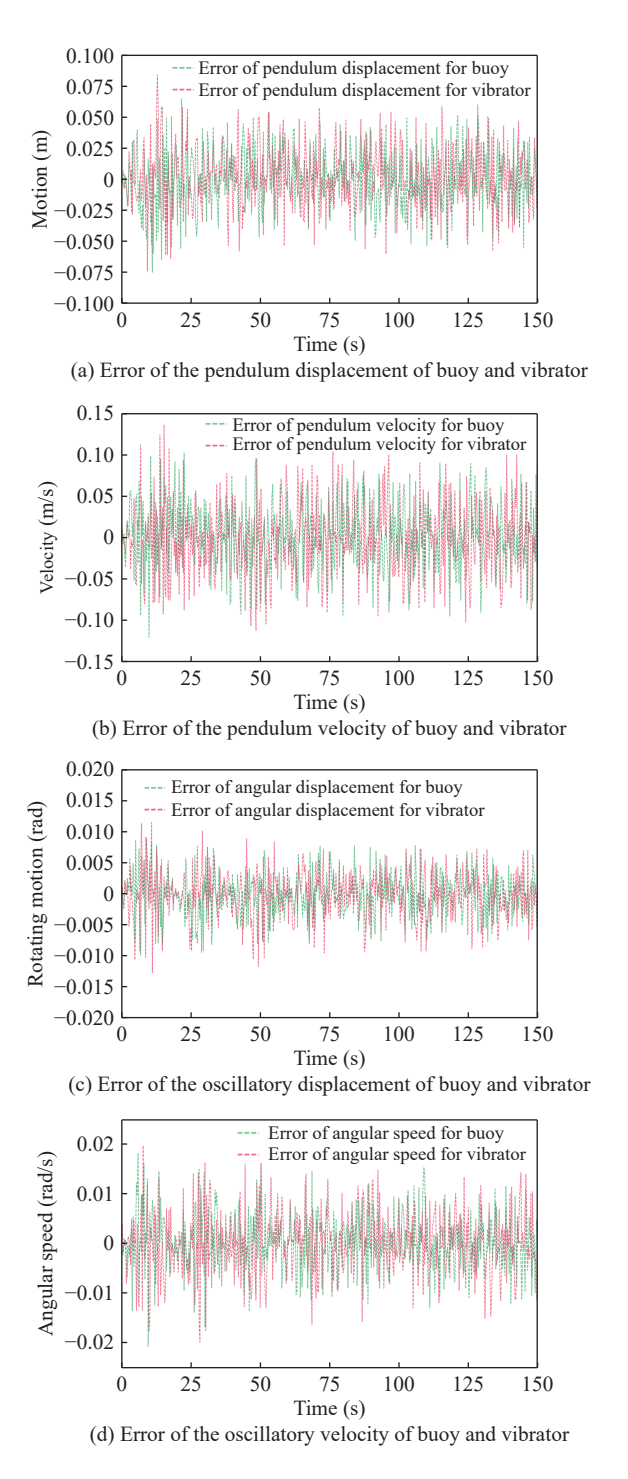


Figure 7 Error between calculated by RK-4 and ground truth concerning pendulum displacement, velocity, oscillatory angular displacement, and velocity of the buyo and vibrator.

The amount of time taken and the capabilities of the machine occupied to run an algorithm are critical indicators to analyze the convergence performance. We record the time consumed to run the two algorithms aforementioned. We conduct the two algorithms for 100 times and record the average time used for running this algorithm for solving the model with uncertainty in the perspective of kinetic characteristic and energy output. Meanwhile, we also demonstrate the RAM utilized for the computation. The proposed DOARK used 2.01 s to run while the time consumed

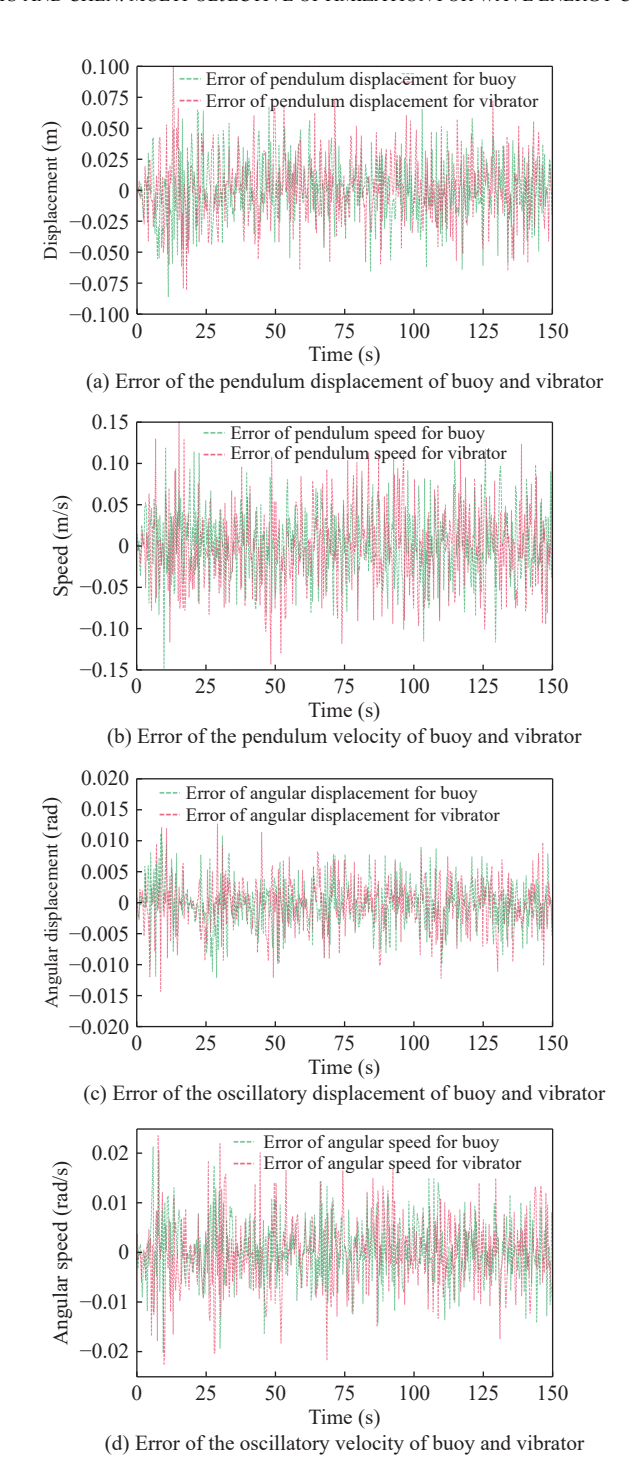


Figure 8 Error between calculated by DOARK and ground truth concerning pendulum displacement, velocity, oscillatory angular displacement, and velocity of the buyo and vibrator.

for running the conventional RK-4 method is 2.28 s. The RAM occupied for conducting the DOARK and RK-4 method are 175.41 and 178.02 MB, respectively. The DOARK realizes the significant enhancement of its accuracy with 1.47% less resources. To sum up, even though taking the complexity into consideration, our proposed DOARK is still ideal in solving the WEC model with fabulous efficiency.

The proposed DOARK algorithm demonstrates significant advantages over the traditional RK method. DOARK dynamically adjusts both the integration step size and the

Table 3 Comparison of MSE between RK-4 method and DOARK.

Item	$RK-4 \\ (1 \times 10^{-5})$	$ DOARK \\ (1 \times 10^{-5}) $
Pendulum displacement of buoy	60.73	55.80
Pendulum displacement of vibrator	71.66	64.97
Pendulum velocity of buoy	177.82	164.71
Pendulum velocity of vibrator	216.35	197.48
Oscillatory angular displacement of buoy	1.32	1.21
Oscillatory angular displacement of vibrator	1.62	1.49
Oscillatory angular velocity of buoy	3.65	3.35
Oscillatory angular velocity of vibrator	4.60	4.21
Average	67.22	61.65

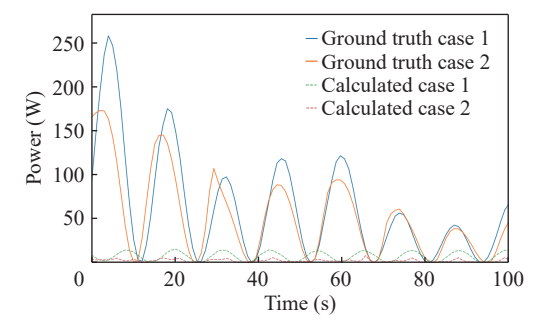


Figure 9 Result of output energy of the optimized WEC model solved with DOARK.

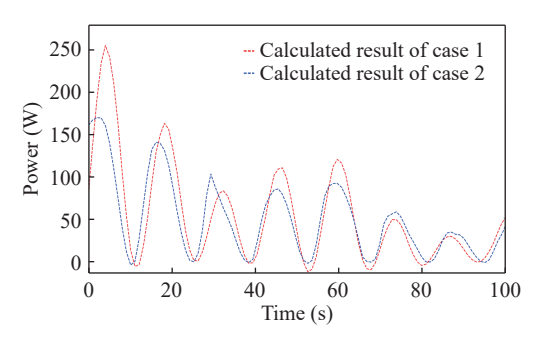


Figure 10 Error changes of the two models within 100 s of DOARK.

Table 4 MSE of output power in case 1 and case 2 calculated by RK-4 and DOARK.

Method	MSE in case 1	MSE in case 2
RK-4	2014.1258	1761.0898
DOARK	1761.0996	1596.8001

order based on local truncation errors and environmental volatility instead of RK, which is based on a fixed step size and order. Specifically, DOARK employs an embedded pair of RK formulas of different orders to estimate the local error at each step and modifies the step size accordingly to keep the error within a predefined threshold. Moreover, in highly dynamic regimes, the algorithm increases the integration order to better resolve stiff or rapidly changing dynamics. While in

smoother regions, it lowers the order to reduce computational cost. This two-level adaptation mechanism allows DOARK to efficiently capture high-frequency and nonlinear system behaviors, while redundant computations during stable conditions are also reduced. Additionally, environmental volatility metrics are used as an auxiliary signal to guide the adjustment process, ensuring context-aware solver behavior. As a result, DOARK achieves an optimal balance between numerical precision and computational efficiency, making it particularly well-suited for simulating complex and uncertainty-driven ocean environments.

To further validate the error control capability of the DOARK method under complex disturbance conditions, we randomly selected 100 time points and added disturbances at five time points to simulate sudden changes in the environment. We selected RKF-45, a typical traditional adaptive RK method, as the comparison object. As shown in Fig. 11, although the errors of both methods remain low in the non-disturbance phase, the DOARK method significantly suppresses the error peaks in each disturbance interval. The maximum error of the RKF-45 method is 194.7 W, while that of the DOARK method is only 119.5 W, which is a reduction of error by 38.6%. The results show that the DOARK method has better adaptive ability and robustness in dealing with nonsmooth inputs and fast perturbation responses, and effectively makes up for the shortcoming of the traditional method in adjusting the step-size lag under transient perturbations.

We assume that damping and restoring forces in the system vary nonlinearly with state changes, which imposes strict requirements on integration accuracy. In particular, sharp and transient dynamics are often missed by traditional Runge-Kutta methods because of their fixed integration structure. To evaluate this, we introduced synthetic high-frequency perturbations at specific time intervals to simulate abrupt wave conditions. The results show that DOARK, with its dynamic order and step-size adjustment mechanism, significantly improves numerical stability and resolution in these disturbed regions, especially near resonance or under sudden excitations. This adaptive flexibility is the key reason for its superior performance in solving the highly nonlinear WEC systems.

In conclusion, the comparison results demonstrate that the proposed DOARK algorithm significantly improves both accuracy and convergence over the conventional fourth-order Runge-Kutta method, and better captures the physical coupling features of the WEC system. In particular, under multiple externally imposed wave disturbances, DOARK consistently yields lower absolute errors compared with RKF-45, with the maximum error reduced from 194.7 to 119.5.

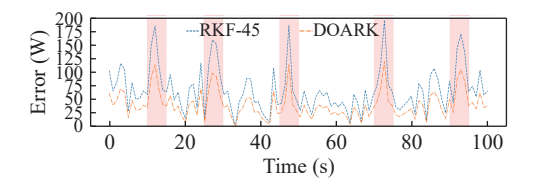


Figure 11 Error change of the RKF-45 and DOARK with disturb added.

This is attributed to its ability to dynamically adjust both step size and integration order, enabling finer resolution near abrupt system changes. Although DOARK incurs moderate computational overhead, it provides greater numerical stability, physical consistency, and robustness under fluctuating marine conditions.

C. Result of Optimization

Figure 12 demonstrates the Pareto solution for the multiobjective optimization in three different scenarios. It can be observed that as the complexity of the wave conditions increases, the systematic damage becomes more intensive, while the output power also increases.

In scenario 1, the unit systematic damage of 64.55 is associated with an output power of 9.54 W. For scenario 2, a similar output power corresponds to a systematic damage value of 128.18, and this number reaches 150.44 in scenario 3.

Moreover, it can be concluded that the upper bound range of both output power and systematic damage expands with increasing complexity.

Consider the two normalized objectives of each Pareto solution acquired based on simulation, \tilde{D} and $\tilde{P} \in [0,1]$, as a two-dimensional vector, with the ideal point at (0,0). The best compromise solution is the point in this vector space that minimizes the L_{∞} norm, such as the Chebyshev distance to the ideal point. Equivalently, it minimizes the worst deviation of both metrics and thus achieves an automatic balance without subjective weighting. Ultimately, the scenario with the largest combined trade-off is chosen to be the best tradeoff solution in the Pareto frontier, which is marked in Fig. 12. Based on the optimal solution in Fig. 12, as the sea state changes over time, the Pareto front of the optimum control problem also evolves. The Pareto front appears steeper in regions where the damage value is low, indicating that greater power output can be achieved with lower damage in these conditions.

This suggests that in rough sea conditions, the system must tolerate greater damage to maintain an output power close to that of a stable sea scenario. This occurs because of the higher availability of wave energy resources, which results in larger wave heights and more volatile wave frequencies.

To cope with increasing systematic damage, a conventional control strategy is employed to stabilize the system. In particular, damper coefficients are adjusted to limit the output power, while parameters related to systematic damage, such as $C_{\rm u}$ and u(t), are reduced to regulate the input energy.

Similarly, coefficients α and β are also controlled. Most of these variables are associated with lower output power, emphasizing the trade-off between energy extraction and structural endurance. Furthermore, excessive mechanical system damage results in low energy generation efficiency. Thus, in the proposed optimization method, coefficients influencing output power and systematic damage are designed to be adjustable.

The results in Fig. 12 support the proposed model's superiority in flexibility, demonstrating its effectiveness in adapting to varying wave conditions.

Figure 13 illustrates the results of the control strategy

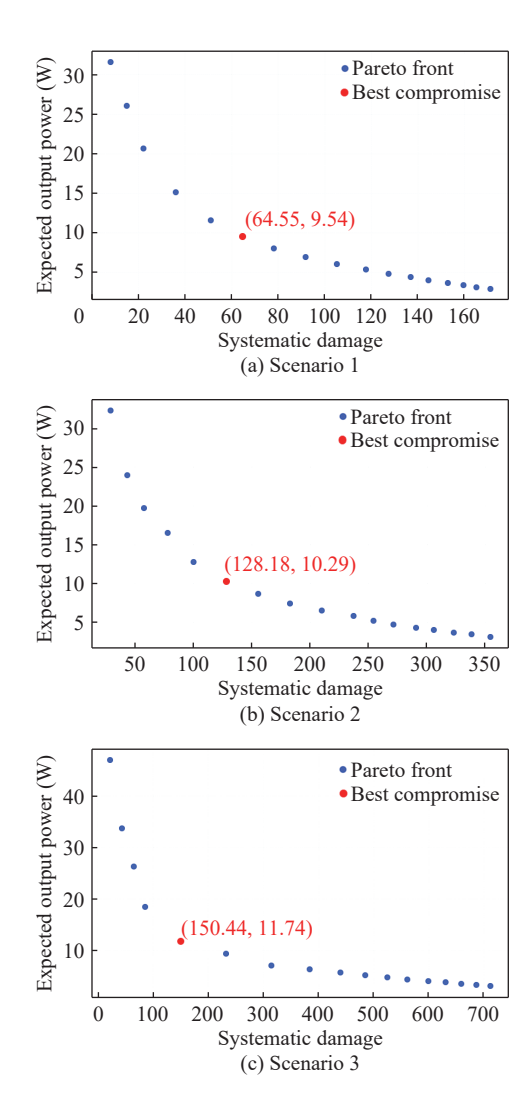


Figure 12 Pareto solution for the multi-objective optimization.

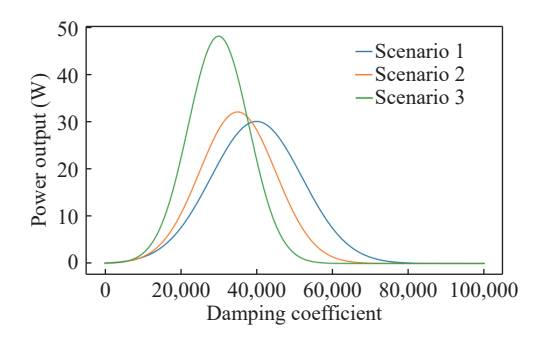


Figure 13 Relationship between the damper coefficient and the output power.

applied to the damper coefficients. Both of the rotation and linear damper obey this founded rule. It can be observed that in volatile sea states, the peak values of output power are achieved with lower damper coefficient values compared with those in stable conditions. However, in scenario 3, the attenuation trend of the output power becomes more pronounced with increasing damper coefficients, which is more significant compared with scenario 1 and scenario 2.

This trend exhibits similarities across both linear and rotary dampers, suggesting a consistent relationship between damper coefficients and output power. Based on the simulation results, it can be inferred that higher damper coefficient values are associated with more intensive systematic damage, and this correlation is more pronounced under complex wave conditions. Furthermore, higher wave volatility is linked to a simultaneous rapid increase in both output power and systematic damage.

Therefore, in scenario 3, which represents a highly unstable condition, a lower damper coefficient strategy is preferred to protect the WEC from excessive damage.

Figure 14 depicts the results of optimization. It can be inferred that the improvement is larger in the volatile operational conditions than that of in stable situations. The output energy is optimized with a level of 12.34% in scenario 3 while the optimizations are 7.52% and 6.71% in scenario 2 and scenario 1, respectively. For systematic damage, the optimization effect is more significant in scenario 3, which possesses a harsh condition. Before the application of multi-objective robust-stochastic strategy, the value of systematic damage is 178.37 and it is 150.44 with strategy applied, which is increased by 15.65%.

The enhancement is mainly attributed to the integration of stochastic uncertainty and dynamic damping adjustments in the model. Thus, more precise control of the wave-induced kinetic behavior is enabled. The results demonstrate the advantage of hybrid integration of stochastic modeling, adaptive numerical solving, and robust control. Traditional models often assume stationary or simplified wave dynamics, leading to over-idealized predictions. In contrast, our method adapts in real time to wave fluctuations, optimizing the trade-off between power capture and structural fatigue.

In particular, the proposed multi-objective robust-stochastic optimization strategy plays a central role in this improvement. It formulates energy output and structural damage as competing objectives within a unified cost function, allowing the controller to dynamically adjust key variables, such as

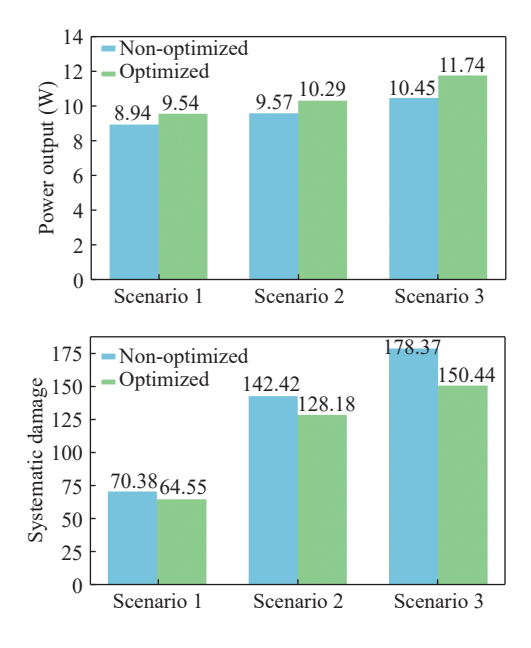


Figure 14 Results of optimization.

damping coefficients and control input in response to evolving sea states. The stochastic terms embedded in the optimization framework simulate realistic ocean disturbances, which guide the search toward control solutions that are not only energy-efficient but also robust against transient shocks. As a result, the optimization systematically drives the system to operate near the power-efficiency frontier while staying within safe dynamic limits, leading to the observed 12.34% increase in output and 15.65% reduction in damage. Therefore, our proposed optimization strategy significantly enhances the adaptability and resilience of WEC systems in volatile marine conditions.

VI. CONCLUSION

This work improves the accuracy of the WEC model in both the perspective of kinetic characteristic and output power. Then, the performance of DOARK improved based on RK-4 is analyzed. Moreover, we conduct optimization for the simultaneous minimization of accumulated damage and maximization of output power. Compared with the previous works, uncertainty is considered based on the introduction of stochastic perturbation term and randomized interference term, which represents the influence of unpredictable conditions in the complex scenarios. It is worthwhile to mention that there is no study to optimize the output energy and systematic damage with multi-objective robust-stochastic strategy. Overall, the model incorporating uncertainty exhibits smaller deviations from the ground truth solutions compared to the initial model. Moreover, the utilization of DOARK decreases the errors between the calculated solution and the ground truth, which means the improved method for solving the differential equation is efficient with higher accuracy and less resources required because of the strategy of adaptive step size adjustment for the different wave conditions with diverse complexity, which balances the accuracy and calculation efficiency. This means the errors are controlled in detail so that the accumulative error in classic RK method is avoided. Furthermore, cost functions are defined for the simultaneous optimization of the output power and systematic damage. For solving the problem of multi-objective, multi-objective robust-stochastic strategy is measured to realize the optimization. Based on the simulation results, the climb of volatility of working conditions of WEC will make the output energy increase but the corresponding damage is also higher than stable scenarios. In scenarios with unstable conditions, despite the output power is limited, a more conventional strategy that controls the parameters to decrease the systematic damage is a reasonable decision for the stability of WEC.

As a direction for future research, we intend to implement the proposed DOARK-based robust-stochastic control framework in field experiments under real ocean conditions. Such validation will help assess the practical applicability of the model and identify potential improvements informed by real-world operational data.

Moreover, the proposed method is structurally adaptable and exhibits strong scalability across different WEC configurations. Specifically, the dynamic modeling

framework is built upon a modular representation of hydromechanical interactions, which allows the integration of additional degrees of freedom without requiring fundamental changes to the control and numerical schemes. The hybrid robust-stochastic control strategy and the DOARK solver are inherently compatible with generalized motion equations, as long as the system dynamics can be expressed in coupled ordinary differential equation form. For example, the model can be extended to multi-body WEC systems, point absorbers with multi-axis PTO units, or oscillating water column devices by updating the governing dynamics and associated damping models. In future work, we will validate this scalability by applying our method to systems with varying structural topologies and PTO types, such as hydraulic or pneumatic PTOs, and assess how control performance and computational efficiency evolve with system complexity. This direction ensures that our approach is not only tailored to the current prototype but also generalizable to a broader class of WEC architectures.

REFERENCES

- J. E. Kim and T. Tang, Preventing early lock-in with technologyspecific policy designs: The renewable portfolio standards and diversity in renewable energy technologies, *Renew. Sustain. Energy Rev.*, 2020, 123, 109738.
- [2] S. Astariz and G. Iglesias, The economics of wave energy: A review, Renew. Sustain. Energy Rev., 2015, 45, 397–408.
- [3] B. G. Reguero, I. J. Losada, and F. J. Méndez, A global wave power resource and its seasonal, interannual and long-term variability, *Appl. Energy*, 2015, 148, 366–380.
- [4] X. Shi, B. Liang, S. Li, J. Zhao, J. Wang, and Z. Wang, Wave energy resource classification system for the China east adjacent seas based on multivariate clustering, *Energy*, 2024, 299, 131454.
- [5] K. Mahmoodi, H. Ghassemi, and H. Nowruzi, Data mining models to predict ocean wave energy flux in the absence of wave records, *Sci. J. Marit. Univ. Szczecin*, 2017, 49(121), 119–129.
- [6] T. Aderinto and H. Li, Conceptual design and simulation of a self-adjustable heaving point absorber based wave energy converter, Energies, 2020, 13(8), 1997.
- [7] D. Clemente, T. Calheiros-Cabral, P. Rosa-Santos, and F. Taveira-Pinto, Hydraulic and structural assessment of a rubble-mound breakwater with a hybrid wave energy converter, J. Mar. Sci. Eng., 2021, 9(9), 922.
- [8] M. C. Devin, D. T. Gaebele, C. A. M. Ströfer, J. T. Grasberger, J. Lee, R. G. Coe, and G. Bacelli, High-dimensional control co-design of a wave energy converter with a novel pitch resonator power takeoff system, *Ocean Eng.*, 2024, 312, 119124.
- [9] E. Al Shami, L. Mayberry, R. Zhang, and X. Wang, A preliminary study of a novel wave energy converter of a Scotch yoke mechanism-based power take-off, *Sustain. Energy Technol. Assess.*, 2023, 60, 103533.
- [10] H. Gao, J. Xiao, and R. Liang, Capture mechanism of a multidimensional wave energy converter with a strong coupling parallel drive, Appl. Energy, 2024, 361, 122828.
- [11] Y. Zhang, Z. Huang, J. Bian, J. Liu, and N. Su, Multi-degree-of-freedom decoupled mechanism for improving energy harvesting performance of wave energy converter, *Energy Convers. Manage.*, 2025, 334, 119850.
- [12] D. Avila, R. Quiza, and G. N. Marichal, An approach for evaluating the stochastic behaviour of wave energy converters, *Appl. Ocean Res.*, 2022, 129, 103372.

- [13] M. Adibzade and H. Akbari, Spectral approach to evaluate multi-body floating wave energy converters in complex sea states, *Ocean Eng.*, 2023, 286, 115567.
- [14] G. Fan, W. Wu, H. Zhang, L. Cui, and F. Blaabjerg, Evaluation of power generation capacity of wave energy converter with a controllable-valve buoy based on wave-to-grid modeling and control, *Ocean Eng.*, 2024, 310, 118519.
- [15] M. H. Jahangir, A. Houmani, and A. Kargarzadeh, A theoretical assessment of energy efficiency of wave tower as an oscillating wave surge converter, *Ocean Eng.*, 2024, 295, 116748.
- [16] C. Quilodrán-Casas, Q. Li, N. Zhang, S. Cheng, S. Yan, Q. Ma, and R. Arcucci, Exploring unseen 3D scenarios of physics variables using machine learning-based synthetic data: An application to wave energy converters, *Environ. Modell. Soft.*, 2024, 177, 106051.
- [17] M. Adibzade and H. Akbari, Fully spectral approach to evaluate the performance of floating wave energy converters in directional complex sea states, *Ocean Eng.*, 2024, 306, 117999.
- [18] H. Mehdipour, E. Amini, S. T. Naeeni, M. Neshat, and A. H. Gandomi, Optimization of power take-off system settings and regional site selection procedure for a wave energy converter, *Energy Convers. Manage. X*, 2024, 22, 100559.
- [19] Z. Zhang, Q. Yu, H. Yang, J. Li, J. Cheng, and S. Gao, Triple-layered chaotic differential evolution algorithm for layout optimization of offshore wave energy converters, *Expert Syst. Appl.*, 2024, 239, 122439.
- [20] M. Zhang, S.-R. Yu, G.-W. Zhao, S.-S. Dai, F. He, and Z.-M. Yuan, Model predictive control of wave energy converters, *Ocean Eng.*, 2024, 301, 117430.
- [21] H. Xu, Y. Zhang, and P. Guo, Effect of various motion modes on the performance of a floating pneumatic wave energy converter with a backward bent duct, *Renew. Sustain. Energy Rev.*, 2025, 217, 115766.
- [22] F. Wang, Q. Ma, Z. Wang, and X. Ding, Stochastic conformal symplectic exponential Runge-Kutta-Nyström integrators for solving damped second-order SDEs with applications in damped stochastic nonlinear wave equations, *Commun. Nonlinear Sci. Numer. Simul.*, 2025, 148, 108874.
- [23] Y. Liu, N. Mizutani, Y.-H. Cho, and T. Nakamura, Nonlinear hydrodynamic analysis and optimization of oscillating wave surge converters under irregular waves, *Ocean Eng.*, 2022, 250, 110888.
- [24] H. Mirzaei, M. N. Moghim, and B. Movahedian, Numerical solution of hydrodynamic efficiency equations for an oscillating water column wave energy converter using the method of fundamental solutions, *Eng. Anal. Bound. Elem.*, 2024, 158, 270–288.
- [25] X.-J. He, J.-S. Li, X.-Y. Huang, and Y.-J. Zhou, Solving elastic wave equations in 2D transversely isotropic media by a weighted Runge-Kutta discontinuous Galerkin method, *Pet. Sci.*, 2023, 20(2), 827–839.
- [26] W. Chen, Z. Huang, Y. Zhang, L. Wang, and L. Huang, Hydrodynamic performance of a three-unit heave wave energy converter array under different arrangement, *Renew. Energy*, 2024, 221, 119808.
- [27] M. K. Hoffmann, G. Moretti, G. Rizzello, and K. Flaßkamp, Multiobjective optimal control for energy extraction and lifetime maximisation in dielectric elastomer wave energy converters, *IFAC-PapersOnLine*, 2022, 55(20), 546–551.
- [28] F. Carapellese, E. Pasta, N. Faedo, and G. Giorgi, Dynamic analysis and performance assessment of the inertial sea wave energy converter (ISWEC) device via harmonic balance, *IFAC-PapersOnLine*, 2022, 55(31), 439–444.
- [29] Y. Cheng, W. Du, S. Dai, C. Ji, M. Collu, M. Cocard, L. Cui, Z. Yuan, and A. Incecik, Hydrodynamic characteristics of a hybrid oscillating water column-oscillating buoy wave energy converter integrated into a π-type floating breakwater, *Renew. Sustain. Energy Rev.*, 2022, 161, 112299.

- [30] A. Shadmani, M. Reza Nikoo, T. Etri, and A. H. Gandomi, A multiobjective approach for location and layout optimization of wave energy converters, *Appl. Energy*, 2023, 347, 121397.
- [31] Y. Cheng, F. Song, C. Xi, M. Collu, Z. Yuan, and A. Incecik, Feasibility of integrating a very large floating structure with multiple wave energy converters combining oscillating water columns and oscillating flaps, *Energy*, 2023, 274, 127301.
- [32] H. Gu, P. Stansby, Z. Zhang, G. Zhu, P. Lin, and H. Shi, Research and concept design of wave energy converter on ocean squid jigging ship, *Energy*, 2023, 285, 129406.
- [33] A. Rahimi, S. Rezaei, S. Mansourzadeh, and J. Parvizian, Dimensional optimization of a two-body wave energy converter under irregular waves for the strait of Hormuz, *Ocean Eng.*, 2024, 292, 116539.
- [34] A. Vakili, A. Pourzangbar, M. M. Ettefagh, and M. Abdollahi Haghghi, Optimal control strategy for enhancing energy efficiency of Pelamis wave energy converter: A simulink-based simulation approach, *Renew. Energy Focus*, 2025, 53, 100685.
- [35] Q. Wei, T. Li, J. Zhang, and F.-Y. Wang, Primal-dual adaptive dynamic programming for finite-horizon optimal control of nonlinear systems with isoperimetric constraints, *Automatica*, 2025, 173, 112029.
- [36] Y. Chen, L. Agostini, G. Moretti, G. Berselli, M. Fontana, and R. Vertechy, Fatigue life performances of silicone elastomer membranes for dielectric elastomer transducers: Preliminary results, in *Proc. of SPIE 10966, Electroactive Polymer Actuators and Devices (EAPAD) XXI*, Denver, CO, USA, 2019, 1096616.
- [37] J. Lu, Q. Wei, and F.-Y. Wang, Parallel control for nonzero-sum games with completely unknown nonlinear dynamics via reinforcement learning, *IEEE Trans. Syst. Man Cybern. Syst.*, 2025, 55(4), 2884–2896.
- [38] E. Giglio, E. Petracca, B. Paduano, C. Moscoloni, G. Giorgi, and S. A. Sirigu, Estimating the cost of wave energy converters at an early design stage: A bottom-up approach, *Sustainability*, 2023, 15(8), 6756.
- [39] Y.-P. Xu, R.-H. Liu, L.-Y. Tang, H. Wu, and C. She, Risk-averse multiobjective optimization of multi-energy microgrids integrated with power-to-hydrogen technology, electric vehicles and data center under a hybrid robust-stochastic technique, *Sustain. Cities Soc.*, 2022, 79, 103699.
- [40] A. Babarit, A database of capture width ratio of wave energy converters, Renew. Energy, 2015, 80, 610–628.
- [41] J. Náprstek, Combined analytical and numerical approaches in dynamic stability analyses of engineering systems, *J. Sound. Vib.*, 2015, 338, 2–41.



Runhao Liu received the BS degree from Inner Mongolia University of Science & Technology, Baotou, China, in 2024. He is currently pursuing the MS degree at Zhejiang University, Hangzhou, China. His research interests include intelligent control, optimization, mathematical modeling, and computational mathematic. He is the author of nearly 10 papers to date, and one of these has been recognized as an ESI highly cited paper. He has also published several patents, demonstrating notable

academic achievements.



Ziming Chen received the BS degree from Inner Mongolia University of Science & Technology, Baotou, China, in 2024. He is currently pursuing the MS degree at East China University of Science and Technology, Shanghai, China. His research interests include information and computational science. He has published several papers patents, which proves his academic ability.